Journal of Computational Physics 227 (2008) 9333–9364

Contents lists available at ScienceDirect

Journal of Computational Physics

journal homepage: www.elsevier.com/locate/jcp

A quasi-positive family of continuous Darcy-flux finite-volume schemes with full pressure support

Michael G. Edwards *, Hongwen Zheng

Civil and Computational Engineering Centre, School of Engineering, Swansea University, Singleton Park Swansea, SA2 8PP Wales, UK

ARTICLE INFO

Article history:
Received 24 February 2007
Received in revised form 18 May 2008
Accepted 22 May 2008
Available online 17 June 2008

Keywords:
Family of flux-continuous schemes
Locally conservative
Finite-volume
Control-volume distributed (CVD)
Multi-point flux approximation (MPFA)
Positivity
Monotonicity
Maximum principle
M-matrix
Full pressure continuity
Anisotropy and pressure equation

ABSTRACT

A new family of flux-continuous, locally conservative, finite-volume schemes is presented for solving the general tensor pressure equation of subsurface flow in porous media. The new schemes have full pressure continuity imposed across control-volume faces. Previous families of flux-continuous schemes are point-wise continuous in pressure and flux.

When applying the earlier point-wise flux-continuous schemes to strongly anisotropic full-tensor fields their failure to satisfy a maximum principle (as with other FEM and finite-volume methods) can result in loss of local stability for high anisotropy ratios which can cause strong spurious oscillations in the numerical pressure solution.

An *M*-matrix analysis reveals the upper limits for guaranteeing a maximum principle for general 9-point schemes and aids in the design of schemes that minimize the occurrence of spurious oscillations in the discrete pressure field.

The full pressure continuity schemes are shown to possess a larger range of flux-continuous schemes, than the previous point-wise counter parts. For strongly anisotropic full-tensor cases it is shown that the full quadrature range possessed by the new schemes permits these schemes to exploit quadrature points (previously out of range) that are shown to minimize spurious oscillations in discrete pressure solutions. The new formulation leads to a more robust quasi-positive family of flux-continuous schemes applicable to general discontinuous full-tensor fields.

1. Introduction

Subsurface flow in porous media is governed by Darcy's law. When formulating a finite-volume pressure equation scheme, continuous normal flux and pressure are key physical constraints that must be imposed at control-volume interfaces, across which strong discontinuities in permeability can occur. Rapid variation in permeability with strong anisotropy are common features in subsurface reservoirs.

The derivation of algebraic flux continuity conditions for full-tensor discretization operators has lead to families of efficient locally conservative flux-continuous control-volume distributed (CVD) finite-volume schemes for determining the discrete pressure and velocity fields in subsurface reservoirs [1,3–11], these schemes are classified by the quadrature parameterization $0 < q \leqslant 1$. Schemes of this type are also called multi-point flux approximation schemes or MPFA [14,15] where focus has been on a scheme that belongs to the above mentioned family with ($q = 1$). Further schemes of this type

* Corresponding author. Tel.: +44 1792 513175.
E-mail address: m.g.edwards@swansea.ac.uk (M.G. Edwards).

0021-9991/$ - see front matter © 2008 Elsevier Inc. All rights reserved.
doi:10.1016/j.jcp.2008.05.028

are presented in [35,16–19]. All of these schemes are applicable to the diagonal and full-tensor pressure equation with generally discontinuous coefficients and remove the O(1) error introduced by standard reservoir simulation schemes when applied to full tensor flow approximation. Coupling of the flux-continuous schemes with higher order convective flux approximations are presented on mixed quadrilateral-triangle grids [12] and on tetrahedra–hexahedra grids with a pyramid interface in [13] respectively. Other schemes that preserve flux continuity have been developed from variational frameworks, using the mixed finite element method (MFE), e.g. [20–25] and related work [26] and discontinuous galerkin methods [27,28], however these schemes require additional degrees of freedom.

When applying these schemes to the elliptic pressure equation with a strongly anisotropic full-tensor field they can fail to satisfy the maximum principle (as with other FEM and finite-volume methods) and result in spurious oscillations in the numerical pressure solution. *M*-matrix conditions were first derived in [1–3], monotone matrix conditions are presented in [30,31]. Grid optimization techniques have also been used to improve stability of the discrete system [32]. Discretization schemes aimed at improving stability are presented in [29,33,41]. Non-linear methods have also been proposed, [10,11] (flux-splitting) and [42] (positivity preserving) both of which have been shown to yield numerical pressure solutions that are free of spurious oscillations.

The *M*-matrix conditions [2,3] define the upper limits for ensuring a local maximum principle is obtained for full-tensor fields. A key condition is that the modulus of the off-diagonal tensor coefficients are bounded by the minimum of the diagonal coefficients. For higher anisotropic ratios, when the resulting discrete matrices violate these bounds these schemes can violate the maximum principle (as with more standard methods) and the numerical pressure solutions can consequently exhibit spurious oscillations.

In this paper a new family of flux-continuous, locally conservative, finite-volume schemes is presented for solving the general tensor pressure equation of subsurface flow in porous media. The new schemes have full pressure continuity imposed across control-volume faces, in contrast to the earlier families of flux-continuous schemes with point-wise continuity in pressure and flux. A full pressure continuity scheme that has helped to motivate this formulation was introduced in [35]. However, the formulation of [35] is derived from linear basis functions and consequently does not extend to a family of schemes. A brief description of the schemes presented here was first given in [3] and initial test results are given in [39]. Since the submission of this paper, a related scheme [38] has also been presented.

The new family of schemes yield improved performance for challenging problems where earlier flux-continuous schemes exhibit strong spurious oscillations. The *M*-matrix analysis leads to an optimal quadrature range for these methods. The degree of freedom within the family of full pressure continuity schemes presented is shown to maximize the quadrature range of the flux-continuous schemes. For strongly anisotropic full-tensor cases where *M*-matrix conditions are violated, it is shown that the earlier families of schemes cannot avoid decoupling of the solution which leads to severe spurious oscillations in the discrete solution. The full quadrature range of the new schemes permits use of quadrature points that were previously out of range for the earlier methods, and that the resulting schemes minimize spurious oscillations in discrete pressure solutions. The new formulation leads to a more robust quasi-positive family of flux-continuous schemes applicable to general discontinuous full-tensor fields.

This paper is organized as follows: Section 2 gives a description of the single phase flow problem encountered in reservoir simulation with respect to the general tensor pressure equation. In Section 3 the formulation of the point-wise continuous triangle pressure support (TPS) flux-continuous finite-volume schemes with discretization in *physical* space is presented. A general CVFE family formulation [2] is presented in Section 4 which motivates the basis functions for the new full pressure support scheme and comparisons between schemes. The family of full pressure support (FPS) schemes is introduced in Section 5. Positivity conditions are presented in Section 6. The relationships between TPS, FPS and CVFE are presented in Section 7 for a spatially constant tensor together with *M*-matrix properties of the schemes. The TPS, FPS quadrature ranges are compared in Section 8, where the crucial advantages of FPS over TPS are given. In Section 9 the TPS schemes are shown to belong to the upper quadrature limit which leads to decoupled solutions, and helps to explain the sensitivity of TPS at high anisotropy ratio. Quasi-positive QM-matrices which are outside of the formal *M*-matrix limits are presented in Section 10. Numerical examples are presented in Section 11, that illustrate benefits and features of the schemes in terms of QM-matrix properties. Conclusions follow in Section 12.

2. Flow equation and problem description

2.1. Cartesian tensor

The problem is to find the pressure ϕ satisfying

$$-\int_{\Omega} \nabla \cdot \mathbf{K}(x,y)\nabla\phi \, \mathrm{d}\tau = \int_{\Omega} q \, \mathrm{d}\tau = \mathbf{M} \tag{1}$$

over an arbitrary domain Ω, subjected to suitable (Neumann/Dirichlet) boundary conditions on boundary $\partial\Omega$, where $\mathbf{V} = -\mathbf{K}\nabla\phi$ is the Darcy velocity. The right hand side term $\mathbf{M}$ represents a specified flow rate and $\nabla = (\partial_x, \partial_y)$. Matrix $\mathbf{K}$ can be a diagonal or full cartesian tensor with general form

$$\mathbf{K} = \begin{pmatrix} K_{11} & K_{12} \\ K_{12} & K_{22} \end{pmatrix}. \tag{2}$$

The full-tensor pressure equation is assumed to be *elliptic* such that

$$K_{12}^2 \leqslant K_{11} K_{22}. \tag{3}$$

The tensor can be discontinuous across internal boundaries of Ω. The boundary conditions imposed here are Dirichlet and Neumann. For incompressible flow pressure is specified at atleast one point in the domain. For reservoir simulation, Neumann boundary conditions on $\partial\Omega$ have zero flux imposed on solid walls such that $(K\nabla\phi)\cdot\hat{n} = 0$, where $\hat{n}$ is the outward normal vector to $\partial\Omega$.

2.2. General tensor equation

The pressure equation is defined above with respect to the *physical* tensor in the initial classical Cartesian coordinate system. Now we proceed to a general curvilinear coordinate system that is defined with respect to a uniform dimensionless transform space with a (ξ, η) coordinate system. Choosing Ω_p to represent an arbitrary control-volume comprised of surfaces that are tangential to constant (ξ, η) respectively, Eq. (1) is integrated over Ω_p via the Gauss divergence theorem to yield

$$-\oint_{\partial\Omega_p} (\mathbf{K}\nabla\Phi)\cdot\hat{\mathbf{n}}\,\mathrm{d}s = \mathbf{M} \tag{4}$$

where $\partial\Omega_p$ is the boundary of Ω_p and $\hat{n}$ is the unit outward normal. Spatial derivatives are computed using

$$\phi_x = J(\phi, y)/J(x, y),\ \phi_y = J(x, \phi)/J(x, y), \tag{5}$$

where $J(x, y) = x_\xi y_\eta - x_\eta y_\xi$ is the Jacobian. Resolving the x, y components of velocity along the unit normals to the curvilinear coordinates (ξ, η), e.g., for ξ = constant, $\hat{\mathbf{n}}\,\mathrm{d}s = (y_\eta, -x_\eta)\,\mathrm{d}\eta$ gives rise to the general tensor flux components

$$F = -\int (T_{11}\phi_\xi + T_{12}\phi_\eta)\,\mathrm{d}\eta, \quad G = -\int (T_{12}\phi_\xi + T_{22}\phi_\eta)\,\mathrm{d}\xi, \tag{6}$$

where general (Piola) tensor $\mathbf{T}$ has elements defined by

$$\begin{aligned} T_{11} &= (K_{11}y_\eta^2 + K_{22}x_\eta^2 - 2K_{12}x_\eta y_\eta)/J, \\ T_{22} &= (K_{11}y_\xi^2 + K_{22}x_\xi - 2K_{12}x_\xi y_\xi)/J, \\ T_{12} &= (K_{12}(x_\xi y_\eta + x_\eta y_\xi) - (K_{11}y_\eta y_\xi + K_{22}x_\eta x_\xi))/J \end{aligned} \tag{7}$$

and the closed integral can be written as

$$\int\int_{\Omega_p} \frac{(\partial_\xi \widetilde{F} + \partial_\eta \widetilde{G})}{J} J\,\mathrm{d}\xi\,\mathrm{d}\eta = \triangle_\xi F + \triangle_\eta G = m, \tag{8}$$

where e.g., $\triangle_\xi F$ is the difference in net flux with respect to ξ and $\widetilde{F} = -(T_{11}\phi_\xi + T_{12}\phi_\eta)$, $\widetilde{G} = -(T_{12}\phi_\xi + T_{22}\phi_\eta)$. Thus any scheme applicable to a full-tensor also applies to non-K-Orthogonal grids. Note that T_{11}, $T_{22} \geqslant 0$ and ellipticity of $\mathbf{T}$ follows from Eqs. (3) and (7). Full tensors can arise from upscaling, unstructured grids and local orientation of the grid and permeability field. For example by Eq. (7), a diagonal anisotropic Cartesian tensor leads to a full-tensor on a curvilinear *orthogonal* grid.

3. Family of flux-continuous finite-volume schemes

Families of flux-continuous locally conservative control-volume distributed (CVD) finite-volume schemes presented in [3–9] have been developed for different grid types including cell-vertex and cell-centred structured and unstructured formulations in physical space and transform space. Numerical convergence rates for a range of quadrature rules in physical space are presented in [9]. We present a summary of the formulation here for the structured cell-centred quadrilateral formulation. (The formulation has also been developed for cell-vertex structured and unstructured grids, e.g. [4,9]). The nine node support of the cell-centred scheme centred on i, j is indicated in Fig. 1(a). The scheme has cell-centred flow and rock variables, so that the approximation points (or nodes) are at the centres of the primal grid cells and the primal grid cells are also the control-volumes over which permeability is defined to be piecewise constant, i.e. in this case control-volume distributed CVD with respect to the primal grid cells. Each group of four cell-centred nodes forms a *dual-cell* Fig. 2, and four triangles are then defined in the *dual-cell* as drawn in Fig. 3, e.g., as in (a) and (b), the position depending on the quadrature point defined below. The *dual-cell* perimeter is defined by joining cell centres with cell edge mid-points as indicated by the dashed contour in Fig. 2(b). The dual cells partition the primal cells (or control-volumes) into sub-cells. Two faces of each sub-cell also coincide with *sub-faces* of the parent control-volume, e.g., faces (S, V_3), (V_3, W) are faces of the sub-cell defined by corner points (i, j), S, V_3, W Fig. 2(a).

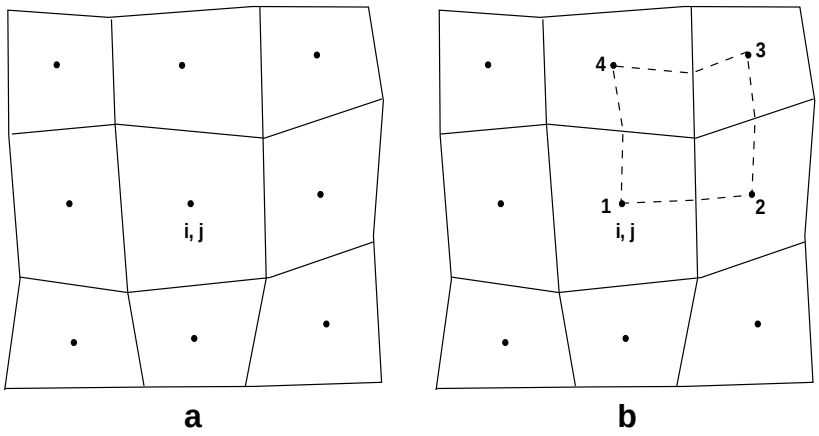

Fig. 1. (a) Nine-node support, cell-centred control-volume i, j. (b) dual-cell dashed line.

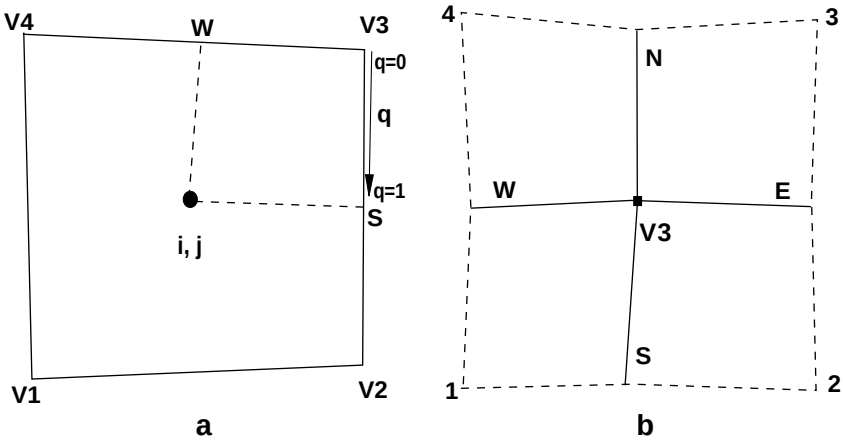

Fig. 2. (a) Cell centre node i, j and 4 vertices $V_1, \ldots, V_4$ of primal cell. (b) Dual cell-centred on V_3, sub-cells and local node numbering over dual-cell.

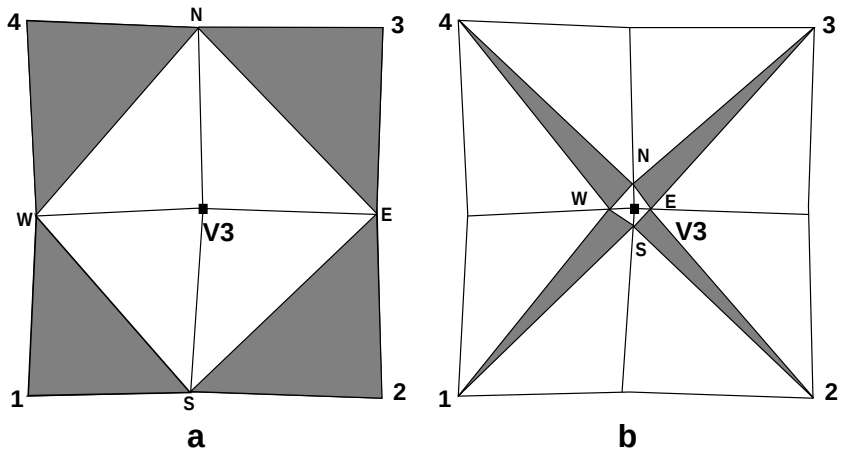

Fig. 3. (a) Standard quadrature, $q = 1$. (b) Example quadrature $q = 0.1$, triangle pressure support.

3.0.1. Family of flux-continuous schemes – quadrature parameterization

Families of flux-continuous schemes are formed when imposing normal flux and pressure continuity conditions on the *sub-faces* where the four shaded triangles meet, at the four positions (N, S, E, W). These points lie on the faces of the sub-cells that are within the perimeter of the dual-cell shown with dashed line in Fig. 2(b). On each *sub-face* the point of continuity is parameterized with respect to the sub-cell face by the variable q where referring to Fig. 2(a) the range of q is given by $(0 < q \leqslant 1]$ with $q = 1$ corresponding to the point of intersection between the sub-faces and the dual-cell perimeter. Hence for a given sub-cell, the points of continuity can lie anywhere in the interval $(0 < q \leqslant 1]$ on the two faces of each sub-cell inside a dual-cell, that coincide with the control-volume *sub-faces*, and the value of q defines the local quadrature point and hence the family of flux-continuous finite-volume schemes. Cell face pressures ϕ_N, ϕ_S, ϕ_E, ϕ_W are introduced at N, S, E, W locations. Pressure sub-triangles are then defined with local triangular support imposed within each quarter (sub-cell) of the *dual-cell* as shown (shaded triangles) in Fig. 3. Pressure ϕ, in local cell coordinates, then assumes a piecewise linear variation over each shaded triangle, with triangular pressure support (TPS).

The parametric variation in q is illustrated further using the sub-cell example of Fig. 2, with sub-cell containing shaded sub-triangle (1, S, W). Let $\mathbf{r}_1 = (x_1, y_1)$ denote the coordinates of the cell-centre and $\mathbf{r}_S = (x_S, y_S)$, $\mathbf{r}_W = (x_W, y_W)$ denote the local continuity coordinates. Then it is understood that the continuity position is a function of q with $\mathbf{r}_S(q)$ and $\mathbf{r}_W(q)$.

Piecewise constant Darcy fluxes are now constructed on each of the pressure sub-triangles belonging to the sub-cells of the *dual-cell*. The local linear pressure ϕ, is expanded in sub-triangle coordinates. The Darcy-flux approximation for sub-triangle (1, S, W) is given below.

$$\begin{pmatrix} \phi_\xi \\ \phi_\eta \end{pmatrix} = \begin{pmatrix} \phi_S - \phi_1 \\ \phi_W - \phi_1 \end{pmatrix} \tag{9}$$

and

$$\begin{pmatrix} x_\xi(q) \\ x_\eta(q) \end{pmatrix} = \begin{pmatrix} x_S(q) - x_1 \\ x_W(q) - x_1 \end{pmatrix}, \quad \begin{pmatrix} y_\xi(q) \\ y_\eta(q) \end{pmatrix} = \begin{pmatrix} y_S(q) - y_1 \\ y_w(q) - y_1 \end{pmatrix}. \tag{10}$$

Using Eqs. (9) and (10) the discrete Darcy velocity is defined as

$$v_h = -\mathbf{K}^1 \nabla \phi_h = -\mathbf{K}^1 \mathbf{G}(q) \begin{pmatrix} \phi_\xi \\ \phi_\eta \end{pmatrix}, \tag{11}$$

where $\mathbf{K}^1$ is the local permeability tensor of cell 1 and dependency of $\nabla \phi_h$ on quadrature point arises through

$$\mathbf{G}(q) \begin{pmatrix} \phi_\xi \\ \phi_\eta \end{pmatrix} = \begin{pmatrix} y_\eta(q) & -y_\xi(q) \\ -x_\eta(q) & x_\xi(q) \end{pmatrix} \frac{1}{J(q)} \begin{pmatrix} \phi_S - \phi_1 \\ \phi_W - \phi_1 \end{pmatrix}, \tag{12}$$

where approximate $\mathbf{r}_\xi(q)$ and $\mathbf{r}_\eta(q)$ are defined by Eq. (10). The normal flux at the left hand side of S (Fig. 2) is resolved along the outward normal vector $\mathrm{d}L_S = \frac{1}{2}((y_{v3} - y_{v2}), -(x_{v3} - x_{v2}))$ and is expressed in terms of the general tensor $T = T(q)$ as

$$F_S^1 = v_h \cdot \mathrm{d}L_S = -(T_{11}^1 \phi_\xi + T_{12}^1 \phi_\eta)|_S^1 \tag{13}$$

where it is understood that the resulting coefficients of $-(\phi_\xi, \phi_\eta)|_S^1$ denoted by $T_{11}|_S^1$ and $T_{12}|_S^2$ are sub-cell (physical-space) approximations of the general tensor components (Eq. (13)) at the left hand face at S, and are functions of q. A similar expression for flux is obtained at the right hand side of S from cell 2 (Fig. 2(b). Similarly sub-cell fluxes are resolved on the two sides of the other faces at E, W and N. Flux continuity is then imposed across the four cell interfaces at the four positions N, S, E and W. (Fig. 3 which are specified according to quadrature point q.)

The *physical* space flux-continuity conditions for cells 1–4, sharing a common grid vertex inside the dual-cell are then expressed as

$$\begin{aligned} F_N &= -(T_{11}\phi_\xi + T_{12}\phi_\eta)|_N^3 = -(T_{11}\phi_\xi + T_{12}\phi_\eta)|_N^4, \\ F_S &= -(T_{11}\phi_\xi + T_{12}\phi_\eta)|_S^1 = -(T_{11}\phi_\xi + T_{12}\phi_\eta)|_S^2, \\ F_E &= -(T_{12}\phi_\xi + T_{22}\phi_\eta)|_E^2 = -(T_{12}\phi_\xi + T_{22}\phi_\eta)|_E^3, \\ F_W &= -(T_{12}\phi_\xi + T_{22}\phi_\eta)|_W^1 = -(T_{12}\phi_\xi + T_{22}\phi_\eta)|_W^4 \end{aligned} \tag{14}$$

The above system of Eq. (14) is then written as the linear system

$$F = A_L \Phi_f + B_L \Phi_v = A_R \Phi_f + B_R \Phi_v, \tag{15}$$

where $F = (F_N, F_S, F_E, F_W)^{\mathrm{T}}$ are the fluxes defined in the dual-cell and $\Phi_f = (\phi_N, \phi_S, \phi_E, \phi_W)^{\mathrm{T}}$ are the interface pressures. Similarly $\Phi_v = (\phi_1, \phi_2, \phi_3, \phi_4)^{\mathrm{T}}$ are the cell centred pressures. Thus the four interface pressures are expressed in terms of the

four cell-centred pressures. Using Eq. (15), Φ_f is now expressed in terms of Φ_v to obtain the dual-cell flux and coefficient matrix

$$F = (A_L(A_L - A_R)^{-1}(B_R - B_L) + B_L)\Phi_v. \tag{16}$$

Thus the cell-face pressures are eliminated from the flux by being determined locally in terms of the cell-centred pressures in a preprocessing step, avoiding introduction of the interface pressure equations into the assembled discretization matrix. Eq. (16) can also be written as

$$AF = -\Delta\Phi_v, \tag{17}$$

where the entries of matrix A are accumulated inverse tensor elements and $\Delta\Phi_v = (\phi_{21}, \phi_{32}, \phi_{34}, \phi_{41})^{\mathrm{T}}$ are the differences of cell-centred pressures, where e.g. $\phi_{21}=\phi_2-\phi_1$. Consistency of the formulation follows from Eq. (17) which shows that flux is zero for constant potential.

The relationship between CVD(MPFA) and the mixed method, first presented in [4] for $q = 1$ (and used in a convergence proof [40]) hinges on Eq. (17). A novel mixed method with similar properties and proven convergence is presented in [19]. The above system of Eq. (17) also represents the generalisation of the standard flux with harmonic coefficients to general elements with families of schemes defined by quadrature point q, see [4,8] for details. Although the physical space families do not posses symmetric discretization matrices for arbitrary quadrilaterals they are positive definite subject to discrete ellipticity of the symmetric part of the tensor [8]. However transform space (cell and sub-cell) formulations that are symmetric positive definite are presented in [3,5,6,8]. Flux continuity in the case of a general-tensor is obtained while maintaining the standard *single* degree of freedom per cell. Since the continuity equations depend on both ϕ_ξ and ϕ_η (unless a diagonal tensor is assumed with cell-face midpoint quadrature resulting in a 2-point flux), the interface pressures $\Phi_f = (\phi_N, \phi_S, \phi_E, \phi_W)^{\mathrm{T}}$ are locally coupled and each group of four interface pressures is determined simultaneously in terms of the group of four cell-centred pressures whose union contains the continuity positions. Finally for a structured grid the scheme is defined by

$$F_{i+1/2,j} - F_{i-1/2,j} + F_{i,j+1/2} - F_{i,j-1/2} = M, \tag{18}$$

where i, j are the integer coordinates of the central quadrilateral cell, Fig. 1 and

$$\begin{aligned} F_{i+1/2,j} &= F_{S_{i+1/2,j+1/2}} + F_{N_{i+1/2,j-1/2}}, \\ F_{i,j+1/2} &= F_{E_{i-1/2,j+1/2}} + F_{W_{i+1/2,j+1/2}}, \end{aligned} \tag{19}$$

where $i + 1/2, j + 1/2$ denote the "integer" coordinates of the top right hand side dual-cell centred on vertex V_3, Fig. 3. The unstructured formulation is presented in, e.g. [4].

In later sections an M-matrix analysis will be presented for a spatially *constant* full-tensor field. The discrete family scheme coefficients for the point-wise continuous triangle pressure support (TPS) schemes are presented in Table 1 for a *spatially constant* full-tensor field where the numbering of coefficients is indicated in Fig. 4.

For a spatially constant tensor the above family of schemes can be related to a simpler family of CVFE schemes given below. This will prove useful in unwrapping some of the underlying properties of the above schemes.

4. CVFE

The purpose of this section is to introduce an approximation framework that is highly influential within the development of the new full pressure continuity family of schemes. The family of symmetric positive definite control-volume finite element (CVFE) full-tensor schemes was first presented in [2], with further properties in [34]. A comparative formalism of the control-volume distributed CVD(MPFA) point-wise continuous family and the CVFE family is also included in [7]. The CVFE framework is quite transparent for spatially constant permeability coefficients and includes all possible single parameter locally conservative constant coefficient 9-point diagonal and full-tensor schemes. For constant coefficients the flux-continuous schemes can be mapped onto the more transparent control-volume finite element CVFE 9-point framework. Such a mapping was demonstrated in [3] for the family of general tensor schemes as a function $\eta = \eta(q)$, where η is a CVFE family basis function parameterization and q is the flux-continuous quadrature parameterization. A diagram illustrating the variations of q and η is given in Fig. 6. The mapping facilitated the M-matrix analysis of the CVD(MPFA) methods [1,3] and links to the cell-wise CVFE M-matrix analysis in [2]. This approach is expanded upon here in performing an M-matrix analysis of the new full pressure continuity schemes.

The family of quadrilateral CVFE fluxes is defined over a primal grid cell if a cell-vertex formulation is employed and is defined over the primal dual-cell if a cell-centred formulation is employed. The CVFE fluxes are derived from a bilinear approximation of pressure and position vector over the cell (or dual-cell) with

$$\phi = (1-\xi)(1-\eta)\phi_1 + \xi(1-\eta)\phi_2 + \xi\eta\phi_3 + (1-\xi)\eta\phi_4, \tag{20}$$

$$\mathbf{r} = (1-\xi)(1-\eta)\mathbf{r}_1 + \xi(1-\eta)\mathbf{r}_2 + \xi\eta\mathbf{r}_3 + (1-\xi)\eta\mathbf{r}_4, \tag{21}$$

where $0 \leqslant \xi, \eta \leqslant 1$ are the local master element coordinates. The resulting fluxes are given by

Table 1
q-Family (TPS) coefficients for constant tensor field

Integer coordinates	Coefficients	Full tensor
i, j	M_{11}	$2(T_{11}+T_{22})-2(T_{11}+T_{22})(\alpha_T+\beta_T E)$
$i+1, j$	M_{12}	$-T_{11}+(T_{11}+T_{22})(\alpha_T+\beta_T E)$
$i+1, j+1$	M_{13}	$-\frac{1}{2}(T_{11}+T_{22})(\alpha_T+\beta_T E)-\frac{T_{12}}{2}$
$i, j+1$	M_{14}	$-T_{22}+(T_{11}+T_{22})(\alpha_T+\beta_T E)$
$i-1, j+1$	M_{15}	$-\frac{1}{2}(T_{11}+T_{22})(\alpha_T+\beta_T E)+\frac{T_{12}}{2}$
$i-1, j$	M_{16}	$-T_{11}+(T_{11}+T_{22})(\alpha_T+\beta_T E)$
$i-1, j-1$	M_{17}	$-\frac{1}{2}(T_{11}+T_{22})(\alpha_T+\beta_T E)-\frac{T_{12}}{2}$
$i, j-1$	M_{18}	$-T_{22}+(T_{11}+T_{22})(\alpha_T+\beta_T E)$
$i+1, j-1$	M_{19}	$-\frac{1}{2}(T_{11}+T_{22})(\alpha_T+\beta_T E)+\frac{T_{12}}{2}$

It is understood that $\alpha_T=\frac{(1-q)}{2(2-q)}$, $\beta_T=\frac{1}{2(2-q)}$ and $E=\frac{T_{12}^2}{T_{11}T_{22}}$. Here E is a measure of ellipticity and it follows that $E\leqslant 1$.

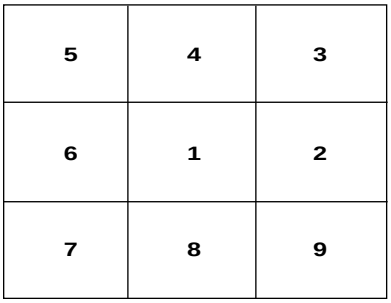

Fig. 4. Numbering of approximation support nodes (stencil).

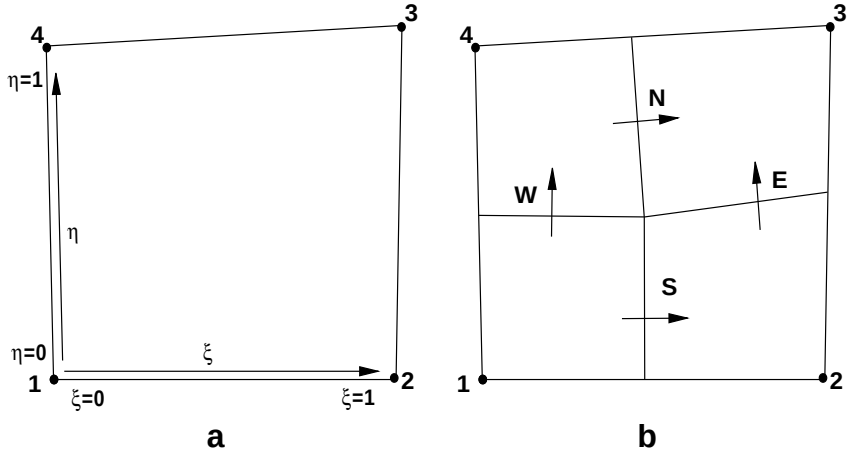

Fig. 5. (a) Local CVFE coordinate system. (b) Local CVFE fluxes.

$$
\begin{aligned}
F_N &= -\frac{1}{2}(T_{11}((\phi_2-\phi_1)(1-\eta)+(\phi_3-\phi_4)\eta)+T_{12}((\phi_4-\phi_1)(1-\xi)+(\phi_3-\phi_2)\xi),\\
F_S &= -\frac{1}{2}(T_{11}((\phi_2-\phi_1)(1-\eta)+(\phi_3-\phi_4)\eta)+T_{12}((\phi_4-\phi_1)(1-\xi)+(\phi_3-\phi_2)\xi),\\
F_E &= -\frac{1}{2}(T_{12}((\phi_2-\phi_1)(1-\eta)+(\phi_3-\phi_4)\eta)+T_{22}((\phi_4-\phi_1)(1-\xi)+(\phi_3-\phi_2)\xi),\\
F_W &= -\frac{1}{2}(T_{12}((\phi_2-\phi_1)(1-\eta)+(\phi_3-\phi_4)\eta)+T_{22}((\phi_4-\phi_1)(1-\xi)+(\phi_3-\phi_2)\xi),
\end{aligned}
\tag{22}
$$

where it is understood that each flux can have its own local coordinates, e.g., $F_S = F_S(\xi_S, \eta_S)$. The range over which each flux is defined is given in Table A.

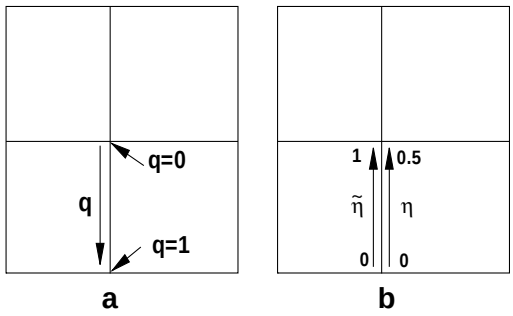

Fig. 6. (a) Variation of q for TPS (b) Variation of $\tilde{\eta}$ for FPS and η for CVFE.

Table A
CVFE fluxes

Flux	ξ	η
F_N	$\frac{1}{2}$	$\frac{1}{2} < \eta \leqslant 1$
F_S	$\frac{1}{2}$	$0 \leqslant \eta < \frac{1}{2}$
F_E	$\frac{1}{2} < \xi \leqslant 1$	$\frac{1}{2}$
F_W	$0 \leqslant \xi < \frac{1}{2}$	$\frac{1}{2}$

In this paper we focus on a single parametric family of schemes. For constant coefficients, the correspondence between the flux-continuous CVD schemes and CVFE schemes is understood through $\xi = \eta = \eta(q)$. The N, S, E, W fluxes correspond with the parametric definition of the 4 control-volume sub-faces that are inside the cell. For example, F_S is defined at a point on the sub-cell control-volume subface Fig. 5, where $\xi_S = 1/2$. Similarly F_E is defined on the adjoining control-volume subface Fig. 5, where $\eta_E = 1/2$ so that

$$\begin{aligned} F_S &= -\frac{1}{2}\left(T_{11}((\phi_2-\phi_1)(1-\eta)+(\phi_3-\phi_4)\eta)+\frac{1}{2}T_{12}((\phi_4-\phi_1)+(\phi_3-\phi_2))\right), \\ F_E &= -\frac{1}{2}\left(\frac{1}{2}T_{12}((\phi_2-\phi_1)+(\phi_3-\phi_4))+T_{22}((\phi_4-\phi_1)(1-\xi)+(\phi_3-\phi_2)\xi)\right), \end{aligned} \tag{23}$$

where the parameter range is defined in Table A with $\xi = \eta$, double parameter families ($\xi \neq \eta$) will be presented in a future report. The analysis is simplified by normalizing the flux parameter range by using the same variable η and the same parameter range ($0 \leqslant \eta < \frac{1}{2}$) for all fluxes and, e.g., the flux pair F_S, F_E are given by

$$\begin{aligned} F_S &= -\frac{1}{2}\left(T_{11}((\phi_2-\phi_1)(1-\eta)+(\phi_3-\phi_4)\eta)+\frac{1}{2}T_{12}((\phi_4-\phi_1)+(\phi_3-\phi_2))\right), \\ F_E &= -\frac{1}{2}\left(\frac{1}{2}T_{12}((\phi_2-\phi_1)+(\phi_3-\phi_4))+T_{22}((\phi_4-\phi_1)\eta+(\phi_3-\phi_2)(1-\eta))\right), \end{aligned} \tag{24}$$

where each flux is defined in it's own local coordinate system and the base schemes of each flux parameterization now correspond with $\eta = 0$. The 9-point scheme coefficients are listed in the CVFE Table 2 where the numbering of coefficients is indicated in Fig. 4.

4.0.2. Flux-continuity and local conservation

We note that CVFE schemes are locally conservative, but not flux continuous; A flux-continuous finite-volume scheme is locally conservative however the converse is not necessarily true and CVFE is a case in point. Of course CVFE is trivially flux-continuous over the control-volume faces [2], but in the CVFE formulation key flux continuity is lacking across the interior interfaces across which the permeability can be discontinuous in the general case. In the M-matrix analysis presented in this paper, schemes are compared for the simplified case of a spatially constant full-tensor field.

5. Family of flux-continuous schemes with full pressure continuity

The family of flux-continuous schemes presented in Section 3 fulfills a number of desirable constraints. However, these schemes are only continuous in pressure and flux in a point-wise sense. Here we introduce a new class of schemes which have continuous pressure support over the entirety of each sub-face. This is achieved by introducing a further interface pressure at the common corner of the four sub-cells as indicated in Fig. 7(a), i.e. at the common primal grid vertex if cell-centred

Table 2
CVFE Family coefficients for constant tensor field

Integer coordinates	Coefficients	Full tensor
i, j	M_{11}	$2(T_{11}+T_{22})-2\eta(T_{11}+T_{22})$
$i+1, j$	M_{12}	$-T_{11}+\eta(T_{11}+T_{22})$
$i+1, j+1$	M_{13}	$-\frac{1}{2}\eta(T_{11}+T_{22})-\frac{1}{2}T_{12}$
$i, j+1$	M_{14}	$-T_{22}+\eta(T_{11}+T_{22})$
$i-1, j+1$	M_{15}	$-\frac{1}{2}\eta(T_{11}+T_{22})+\frac{1}{2}T_{12}$
$i-1, j$	M_{16}	$-T_{11}+\eta(T_{11}+T_{22})$
$i-1, j-1$	M_{17}	$-\frac{1}{2}\eta(T_{11}+T_{22})-\frac{1}{2}T_{12}$
$i, j-1$	M_{18}	$-T_{22}+\eta(T_{11}+T_{22})$
$i+1, j-1$	M_{19}	$-\frac{1}{2}\eta(T_{11}+T_{22})+\frac{1}{2}T_{12}$

and at the centre of gravity of the primal-cell if the formulation is cell-vertex. This enables a bilinear support in pressure to be introduced over each sub-cell so that *full pressure continuity* is achieved over the faces of each control-volume. The bilinear support retains a degree of freedom in position of flux continuity on a subface, and is motivated in part by the generality of the CVFE framework of Section 4, however it is emphasized here that the following schemes are designed to be flux-continuous over the control-volume faces that separate the piecewise constant variation in permeability field, leading to a new family of flux-continuous schemes with full pressure support FPS.

The extra degree of freedom in pressure connecting the four sub-cells of the dual-cell requires an additional constraint equation per dual-cell. Here we employ a similar approach to that of [35] and solve for the additional degree of freedom by imposing the discrete integral form of Eq. (1) to hold over the dual-cell centre. For incompressible flow away from a source/sink this effectively ensures that the dual-cell is divergence free. In order to define the additional dual-cell divergence approximation an auxiliary control-volume surrounding the dual-cell centre is introduced as indicated by any of the dot-dashed lines in Fig. 7(b). Details for the cell-centred formulation follow below.

5.1. Family of CVD(MPFA) full pressure continuity schemes – quadrature parameterization

In this formulation the *lower-case* indices (n, s, e, w) indicate the mid-points of the primal grid cell faces, that are connected to the dual-cell mid-point m forming the interior sub-cell faces. After introduction of a further interface pressure at the common corner m of the four sub-cells (i.e. at the dual-cell centre) indicated in Figs. 7, 8, the set of local interface pressures to be determined over the dual-cell is given by $\Phi_f = (\phi_n, \phi_s, \phi_e, \phi_w, \phi_m)^{\mathrm{T}}$. A sub-cell bilinear approximation of pressure and position vector is introduced locally over each sub-cell with local parametric coordinates $(0 \leqslant \tilde{\xi}, \tilde{\eta} \leqslant 1)$, from which approximate derivatives are derived over each sub-cell. For example over sub-cell 1 Fig. 7(a), (with corners labeled anti-clockwise (1, s, m, w)) we obtain

$$\begin{aligned} \phi_{\tilde{\xi}} &= (1-\tilde{\eta})(\phi_s - \phi_1) + \tilde{\eta}(\phi_m - \phi_w), \\ \phi_{\tilde{\eta}} &= (1-\tilde{\xi})(\phi_w - \phi_1) + \tilde{\xi}(\phi_m - \phi_s), \end{aligned} \tag{25}$$

and

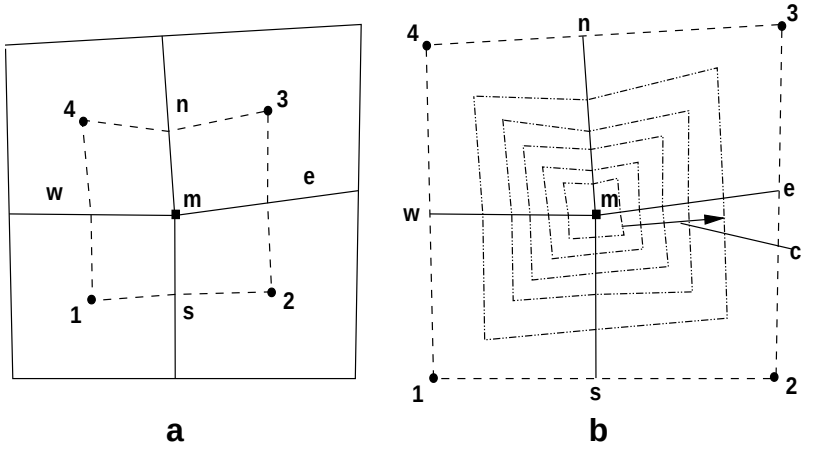

Fig. 7. (a) FPS Dual-cell (dashed) with auxiliary pressure nodes n, s, e, w, m and sub-cells (1, s, m, w), (s, 2, e, m), (m, e, 3, n), (w, m, n, 4) (b) Example range of auxiliary Control-volumes (dot-dashed) centred on m.

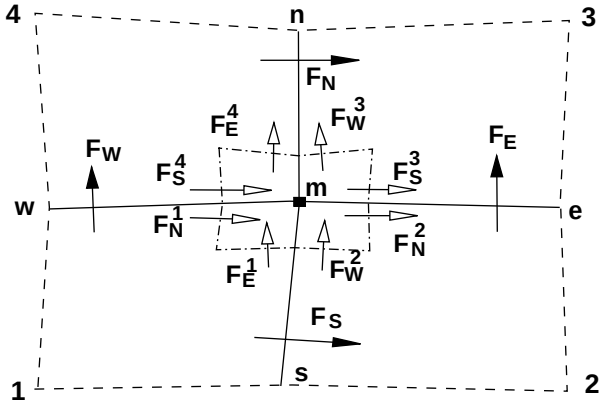

Fig. 8. Fluxes in dual-cell: solid arrow = primal-flux, hollow arrow = auxiliary control-volume flux.

$$\begin{aligned}\mathbf{r}_{\tilde{\xi}} &= (1-\tilde{\eta})(\mathbf{r}_s-\mathbf{r}_1)+\tilde{\eta}(\mathbf{r}_m-\mathbf{r}_w),\\ \mathbf{r}_{\tilde{\eta}} &= (1-\tilde{\xi})(\mathbf{r}_w-\mathbf{r}_1)+\tilde{\xi}(\mathbf{r}_m-\mathbf{r}_s).\end{aligned} \tag{26}$$

As in the TPS formulation *upper-case N, S, E, W* define the flux positions of the family of FPS schemes on the control-volume sub-faces. However, unlike the TPS formulation the FPS interface pressures (ϕ_n, ϕ_s, ϕ_e, ϕ_w) remain attached to the mid-points of the primal grid cell faces. The flux continuity conditions of Eq. (14) are now redefined using the above approximate derivatives of ϕ and $\mathbf{r}$ given in Eqs. (25) and (26) which replace that of Eqs. (9) and (10). The family of schemes is defined by a symmetric position of flux continuity parameterized by the local basis function $\tilde{\eta}$, with respect to pairs of sub-cell faces. The FPS flux position is later expressed in terms of the CVFE parameter η where $\eta=\tilde{\eta}/2$ (shown later) and with respect to the TPS parameter q, with $\eta=(1-q)/2$ so that the interval of FPS flux integration $0\leqslant\eta<\frac{1}{2}$ can be readily compared with CVFE and TPS, c.f. Fig. 6. This aids the comparison between TPS, CVFE and FPS schemes presented below. To clarify notation, for example F_S will denote a flux at a quadrature point that may either coincide with s or be between s and m, but never coincides with m, i.e. $0\leqslant\tilde{\eta}<1$ or $1\geqslant q>0$ or equivalently $0\leqslant\eta<\frac{1}{2}$. The additional discrete divergence condition for determining ϕ_m is added to the four interface continuity conditions leading to the local algebraic system

$$\begin{aligned}&F_N=-(T_{11}\phi_{\tilde{\xi}}+T_{12}\phi_{\tilde{\eta}})|_N^3=-(T_{11}\phi_{\tilde{\xi}}+T_{12}\phi_{\tilde{\eta}})|_N^4,\\ &F_S=-(T_{11}\phi_{\tilde{\xi}}+T_{12}\phi_{\tilde{\eta}})|_S^1=-(T_{11}\phi_{\tilde{\xi}}+T_{12}\phi_{\tilde{\eta}})|_S^2,\\ &F_E=-(T_{12}\phi_{\tilde{\xi}}+T_{22}\phi_{\tilde{\eta}})|_E^2=-(T_{12}\phi_{\tilde{\xi}}+T_{22}\phi_{\tilde{\eta}})|_E^3,\\ &F_W=-(T_{12}\phi_{\tilde{\xi}}+T_{22}\phi_{\tilde{\eta}})|_W^1=-(T_{12}\phi_{\tilde{\xi}}+T_{22}\phi_{\tilde{\eta}})|_W^4,\\ &-\sum_{\partial\Omega_{\mathrm{AUX}}}(\mathbf{K}\nabla\Phi)\cdot\hat{\mathbf{n}}\Delta s=0.\end{aligned} \tag{27}$$

Here we illustrate discrete flux continuity for the second equation of Eq. (27), at a point S between s and m with

$$\begin{aligned}F_S&=-(T_{11}^1((1-\tilde{\eta})(\phi_s-\phi_1)+\tilde{\eta}(\phi_m-\phi_w)+T_{12}^1(\phi_m-\phi_s))\\ &=-(T_{11}^2((1-\tilde{\eta})(\phi_2-\phi_s)+\tilde{\eta}(\phi_e-\phi_m)+T_{12}^2(\phi_m-\phi_s)),\end{aligned} \tag{28}$$

where for the left hand side flux, approximations of $\phi_{\tilde{\xi}}$ and $\phi_{\tilde{\eta}}$ are given by Eq. (25). Analogous sub-cell approximations are constructed for each of the flux continuity conditions in Eq. (27). The alternative q parameterization of flux continuity is given by

$$\begin{aligned}F_S&=-(T_{11}^1(q(\phi_s-\phi_1)+(1-q)(\phi_m-\phi_w)+T_{12}^1(\phi_m-\phi_s))\\ &=-(T_{11}^2(q(\phi_2-\phi_s)+(1-q)(\phi_e-\phi_m)+T_{12}^2(\phi_m-\phi_s)).\end{aligned} \tag{29}$$

Referring now to the auxiliary control-volume (perimeter shown dot-dashed) centred on the auxiliary node m of Fig. 8 the auxiliary control-volume is comprised of 4 *sub-subcells* one in each sub-cell. The discrete approximation of the 5th equation in the set of Eq. (27) which represents the local auxiliary divergence condition is constructed in an analogous procedure to that of the primary control-volume approximation of divergence, with eight fluxes one per subface of the auxiliary control-volume. Since the auxiliary control-volume faces lie inside the primary control-volumes where permeability is piecewise constant, the auxiliary control-volume approximation is based on the CVFE formulation. The auxiliary control-volume fluxes are parameterized with $1\geqslant p>0$, where p is a free parameter that defines the local auxiliary flux quadrature, although $p=q$ is one possibility. Note that the auxiliary control-volume can lie in or on the dual-cell, the

Table 3
q-Family (FPS) coefficients for constant tensor field

Integer coordinates	Coefficients	Full tensor
i, j	M_{11}	$2(T_{11}+T_{22}) - 2(T_{11}+T_{22})(\alpha_F + \beta_F ER)$
$i+1, j$	M_{12}	$-T_{11} + (T_{11}+T_{22})(\alpha_F + \beta_F ER)$
$i+1, j+1$	M_{13}	$-\frac{1}{2}(T_{11}+T_{22})(\alpha_F + \beta_F ER) - \frac{T_{12}}{2}$
$i, j+1$	M_{14}	$-T_{22} + (T_{11}+T_{22})(\alpha_F + \beta_F ER)$
$i-1, j+1$	M_{15}	$-\frac{1}{2}(T_{11}+T_{22})(\alpha_F + \beta_F ER) + \frac{T_{12}}{2}$
$i-1, j$	M_{16}	$-T_{11} + (T_{11}+T_{22})(\alpha_F + \beta_F ER)$
$i-1, j-1$	M_{17}	$-\frac{1}{2}(T_{11}+T_{22})(\alpha_F + \beta_F ER) - \frac{T_{12}}{2}$
$i, j-1$	M_{18}	$-T_{22} + (T_{11}+T_{22})(\alpha_F + \beta_F ER)$
$i+1, j-1$	M_{19}	$-\frac{1}{2}(T_{11}+T_{22})(\alpha_F + \beta_F ER) + \frac{T_{12}}{2}$

It is understood that $\alpha_F = \frac{(1-q)}{2}, \beta_F = \frac{cq}{2(q+pc-c)}, R = \frac{H_M}{A_R}$ which is the ratio of the harmonic mean to arithmetic mean of diagonal coefficients T_{11}, T_{22} where $H_M = 2\frac{T_{11}T_{22}}{T_{11}+T_{22}}, A_R = \frac{T_{11}+T_{22}}{2}$ and therefore $R \leqslant 1$, and as before (for the TPS scheme) $E = \frac{T_{12}^2}{T_{11}T_{22}}$ is an ellipticity measure and it follows that $ER \leqslant 1$.

actual size of the auxiliary control-volume is a further degree of freedom to be chosen within the scheme, and is parameterized by the variable $1 \geqslant c > 0$, where $c = 1$ corresponds to an auxiliary control-volume that matches the dual-cell and as $c \to 0$ the auxiliary control-volume tends to zero. The primal control-volume and auxiliary control-volume fluxes are indicated in Fig. 8, with solid arrows for primal fluxes and hollow arrows for auxiliary fluxes. The auxiliary fluxes have super-fixes indicating the auxiliary sub-cell and compass suffices indicating position relative to the primal sub-cell in which they are defined. For example referring again to sub-cell 1 (corners 1, s, m, w), the auxiliary control-volume flux F_N^1 is defined on the top left sub-subcell face by

$$F_N^1 = c(-T_{11}^1(c(1-p)(\phi_s - \phi_1) + (1 - c(1-p))(\phi_m - \phi_w)) - T_{12}^1(c(\phi_w - \phi_1) + (1-c)(\phi_m - \phi_s))) \tag{30}$$

which is a function of the auxiliary quadrature and control-volume size parameters p and c respectively and the tensor here is defined with respect to the auxiliary sub-cell. In the general case this formulation leads to a multiple family of schemes which are functions of the main flux continuity point parameter q, the auxiliary control-volume flux parameter p and auxiliary control-volume size parameter c.

The degrees of freedom of the five equation system Eq. (27) are the five interface pressures $\Phi_f = (\phi_n, \phi_s, \phi_e, \phi_w, \phi_m)^{\mathrm{T}}$ and the four primal cell-centred pressures $\Phi_c = (\phi_1, \phi_2, \phi_3, \phi_4)^{\mathrm{T}}$. The system of equations is rearranged in a similar form to Eq. (15) viz

$$\mathbf{F} = A_L^{5X5}\Phi_f + B_L^{5X4}\Phi_c = A_R^{5X5}\Phi_f + B_R^{5X4}\Phi_c \tag{31}$$

where A_L^{5X5}, A_R^{5X5} are 5X5 matrices and B_L^{5X4}, B_R^{5X4} are 5X4 matrices. Since we only require the four fluxes, we let A_L^{4X5} denote the first four rows of matrix A_L^{5X5} and B_L^{4X4} denote the first four rows of matrix B_L^{5X4}.

The dependence on Φ_f is removed via Eq. (31) and the continuous fluxes of the families of FPS schemes are now expressed in terms of Φ_c with

$$\mathbf{F} = (A_L^{4X5}(A_L^{5X5} - A_R^{5X5})^{-1}(B_R^{5X4} - B_L^{5X4}) + B_L^{4X4})\Phi_c$$

The fluxes are then assembled and discrete divergence is formed as in Eqs. (18) and (19). For a spatially constant tensor field on a logically rectangular grid the family of full pressure support (FPS) schemes reduce to 9-point schemes with coefficients given in Table 3.

6. Positivity and *M*-matrices

The families of flux-continuous schemes TPS and FPS both result in a discrete matrix which forms 5–9 row entries in 2D and 7–27 row entries in 3D on a structured grid. The discrete systems can be written as

$$\mathbf{A}\phi = b, \tag{32}$$

where $\mathbf{A}$ is the discrete matrix operator, ϕ is the unknown pressure and b is the source term. Ideally the discrete system of Eq. (32) should be *monotone*, and satisfy a *maximum principle* that is analogous to that of the continuous counterpart of the discrete problem and hence ensuring that the numerical solution is free from nonphysical oscillations. The discrete matrix operator $\mathbf{A}$ is *monotone* if and only if $\mathbf{A}$ is non-singular and it obeys the following condition [37]

$$\mathbf{A}^{-1} \geqslant \mathbf{O}, \tag{33}$$

where $\mathbf{O}$ is a zero matrix. While a monotone discretization matrix ensures that a non-negative source and boundary data yields a non-negative pressure field, it has not been proven that a monotone discretization matrix will prevent discrete spurious local extrema occurring in the discrete solution of the general tensor pressure equation. A sufficient condition for a maximum principle (which can ensure that no spurious extrema occur in the discrete solution) is that $\mathbf{A}$ is an $\mathbf{M}-$ matrix, i.e. monotone or positive definite with $a_{i,j} \leqslant 0$, $i \neq j$.

6.0.1. Conditions for an M-matrix

The following set of conditions are often easier to verify;
A is an *M*-matrix if

$$\begin{aligned} &a_{i,i} > 0 \quad \forall i, \\ &a_{i,j} \leqslant 0 \quad \forall i,j, \quad i \neq j, \\ &\Sigma_j a_{i,j} \geqslant 0 \quad \forall i. \end{aligned} \tag{34}$$

In addition **A** must be either strictly diagonally dominant (strict inequality in the latter of Eq. (34)) or weakly diagonally dominant with strict inequality for at least one row, **A** must also be irreducible.

Use of the term monotonicity is too strong when describing multi-dimensional solutions, as the local solution can often have a saddle point in structure. For example, for a locally constant tensor field (and zero source) Eq. (1) reduces to $-\tilde{K}_{11}\phi_{\tilde{x}\tilde{x}} - \tilde{K}_{22}\phi_{\tilde{y}\tilde{y}} = 0$ with respect to principal axes $(\tilde{x}, \tilde{y})$, so that $\phi_{\tilde{x}\tilde{x}} = -\tilde{K}_{22}\phi_{\tilde{y}\tilde{y}}/\tilde{K}_{11}$, from which it follows that $\phi_{\tilde{x}\tilde{x}}\phi_{\tilde{y}\tilde{y}} < 0$ leading to the condition for a saddle point with $\phi^2_{\tilde{x}\tilde{y}} \geqslant \phi_{\tilde{x}\tilde{x}}\phi_{\tilde{y}\tilde{y}}$. Here we introduce the term positivity as defined below.

6.1. Positivity

For the *i*th equation of Eq. (32), away from any source or sink, it follows that

$$\phi_i = -\frac{1}{a_{ii}} \sum_{j(i \neq j)} a_{ij}\phi_j. \tag{35}$$

If **A** is an *M*-matrix, by consistency for a constant potential field it follows from Eq. (35) that each non-specified ϕ_i is a convex average of its connecting neighbours. Thus each ϕ_i is bounded between the maximum and minimum of connecting neighbours, such a condition is consistent with the absence of spurious oscillations and defines a local discrete maximum principle. When **A** is an *M*-matrix Eq. (35) defines a positive scheme where the weights of ϕ_j are *positive* and sum to unity.

The first *M*-matrix analysis for schemes of this type is presented in [1–3], where conditions for nine-node flux-continuous schemes to be an *M*-Matrix are

$$\min(T_{1,1}, T_{2,2}) \geqslant \eta(T_{1,1} + T_{2,2}) \geqslant |T_{1,2}| \tag{36}$$

and η is a function of quadrature point. One of the essential conditions here is that

$$|T_{1,2}| \leqslant \min(T_{1,1}, T_{2,2}), \tag{37}$$

which is only *sufficient for ellipticity* [1] and therefore quite limiting on the range of tensors that are applicable. Tensors that are elliptic with

$$T^2_{1,2} \leqslant T_{1,1}T_{2,2} \tag{38}$$

and are such that $|T_{1,2}| > \min(T_{1,1}, T_{2,2})$ violate the *M*-Matrix criteria of Eq. (36) and expose the *M*-Matrix limit.

Numerical examples are presented in the results section where the maximum principle is violated and in these cases the methods do not possess an *M*-matrix or a monotone matrix. Examples are presented for both TPS and FPS flux-continuous finite-volume CVD(MPFA) schemes.

6.2. Related work on stability

In many cases discrete stable solutions of second order elliptic full tensor partial differential equations that are free of spurious oscillations can be computed with schemes that do not necessarily obey the *M*-matrix conditions needed to ensure a maximum principle. In [31] rather than an *M*-matrix, a monotone matrix is pursued for monotonicity. The authors present a detailed analysis to derive the conditions that are sufficient for the matrix to be monotone. Plots of monotone matrix regions are given in the tensor coefficient plane [31] expressed in terms of the minimum diagonal tensor coefficient versus the absolute off-diagonal tensor coefficient, normalized with respect to the maximum diagonal tensor coefficient. While this is an interesting viewpoint, as discussed above, it has not been proven that a monotone matrix will ensure a discrete solution is obtained without spurious oscillations. Such a solution can be obtained if the matrix is an *M*-matrix. A monotone matrix is an *M*-matrix if the off-diagonal coefficients are not positive and thus a monotone matrix is only part of the condition required for a discrete maximum principle as discussed above. From the monotone matrix conditions together with the negative inequality conditions for off-diagonals (i.e. *M*-matrix conditions), [31] goes on to arrive at the same *M*-matrix bounds as first presented in [2,3] (in slightly different notation). An optimal scheme is also identified which corresponds to the quadrature point defined by Eq. (46), first presented in [3]. We illustrate the *M*-matrix conditions of the schemes presented here in the tensor coefficient plane further below.

However, the major challenge to all schemes occurs when the crucial sufficient *M*-matrix condition of Eq. (37) is violated, i.e. when $(\min(T_{1,1}, T_{2,2})^2 < T^2_{1,2} \leqslant T_{1,1}T_{2,2})$. In this case the schemes do not have *M*-matrices or monotone matrices. Four

types of discretization have been proposed to date to overcome this limitation; The first two involve constructing the discrete approximation based on that resulting from the optimal point defined by Eq. (46), either by special case triangulation according to anisotropy angle [33] or by special case construction also according to anisotropy [41]. The second two approaches involve non-linear flux approximation, either by flux-splitting with an imposed maximum principle [10,11] or by a local positivity preserving approximation [42]. The approach adopted here involves using the optimal point of Eq. (46) as a quadrature point. The analysis below shows that the optimal quadrature point can be selected by the FPS and CVFE families for all elliptic tensors, but when strong full-tensor anisotropy is present the optimal point is outside the TPS quadrature range.

First the relationship between the new full pressure support FPS family, the original triangle pressure support (TPS) family and control-volume finite element (CVFE) family is presented for the case of spatially constant full-tensor coefficients.

7. Relationship between TPS, FPS and CVFE for a spatially constant tensor

A correspondence (or mapping) between the flux-continuous CVD family coefficients and the CVFE family coefficients is now established for a spatially constant general full-tensor field. By definition since the general full-tensor is assumed to be spatially constant, there is no need to take account of discontinuous coefficients (fluxes are automatically continuous) and the analysis simplifies considerably. However the construction of triangle pressure support (TPS) and full pressure support (FPS) in the case of constant tensor coefficients still yields families of schemes with distinct properties. The mapping between schemes enables us to understand important consequences of the different discretizations, basically from a single analysis which is verified by practical examples.

In this case the CVD(MPFA) flux-continuous (TPS) and (FPS) schemes take the same form as the family of CVFE schemes. For a spatially constant full tensor the schemes take the common form

$$-\Big(T_{11}(\phi_{i+1,j}-2\phi_{i,j}+\phi_{i-1,j})+T_{22}(\phi_{i,j+1}-2\phi_{i,j}+\phi_{i,j-1})+\frac{T_{12}}{2}(\phi_{i+1,j+1}-\phi_{i-1,j+1}+\phi_{i-1,j-1}-\phi_{i+1,j+1})$$
$$+\frac{\eta}{2}(T_{11}+T_{22})(4\phi_{i,j}-2(\phi_{i+1,j}+\phi_{i-1,j}+\phi_{i,j+1}+\phi_{i,j-1})+\phi_{i+1,j+1}+\phi_{i-1,j+1}+\phi_{i-1,j-1}+\phi_{i+1,j-1})\Big), \tag{39}$$

where the latter difference term of Eq. (39) multiplying $\frac{\eta}{2}(T_{11}+T_{22})$ is a mixed fourth derivative approximation. The nature of η in this term governs the actual difference between the schemes for a constant general full-tensor field. The coefficients of the respective TPS and FPS families are given in Tables 1 and 3 above, for a spatially constant full-tensor field. The coefficients of the CVFE family are given in Table 2. Inspection of Eq. (39) and comparison between Tables 1–3 shows that for a constant tensor the flux-continuous schemes *map* on to the CVFE scheme for specific functional definitions of $\eta = \eta(q)$ as shown below. We also note that since the CVFE family is symmetric positive definite see Appendix 1, it follows from the mappings below that the TPS and FPS families of schemes are therefore symmetric positive definite for spatially constant elliptic tensor coefficients for $\eta < 1/2$.

7.1. Triangle pressure support TPS

For the TPS schemes (compare Tables 1 and 2) the mapping corresponds with η in the CVFE scheme defined by

$$\eta(q) = \alpha_T + \beta_T E = \frac{(1-q)}{2(2-q)} + \frac{1}{2(2-q)}E, \tag{40}$$

where α_T, β_T and E are defined in Section 3 and from which it follows that $\alpha_T + \beta_T E \leqslant 1/2$.

7.2. Full pressure support FPS

For the FPS schemes (compare Tables 3 and 2) the mapping corresponds with η in the CVFE scheme defined by

$$\eta(q) = \alpha_F + \beta_F ER = \frac{(1-q)}{2} + \frac{cq}{2(q+pc-c)}ER, \tag{41}$$

where α_F, β_F and ER are defined in Section 5 and from which it follows that $\alpha_F + \beta_F ER \leqslant 1/2$. Thus both schemes are within the range of the CVFE η family. The η family embodies *all* single parameter 9-point schemes, reduced support schemes and the subordinate 7-point schemes. This is made clear below. Therefore an M-matrix analysis of the CVFE family with coefficients in Table 2 is directly applicable to the TPS and FPS families with coefficients of Tables 1 and 3 via the relationship given by Eqs. (40) and (41) and is performed below.

7.3. Cell-wise M-matrix conditions

An M-matrix test is easily conducted by considering cell-wise (or dual-cell for cell-centred) assembly of fluxes and performing a cell-wise M-matrix analysis following [2]. We note that for CVFE permeability is piecewise constant per-cell so that for piecewise constant T this analysis applies to the fully discrete CVFE method, but the relationship to TPS and FPS only

holds for a spatially constant field. Here we perform a cell-wise M-matrix test for the family (Fig. 10), where, e.g., for the control-volume centred on local node 2, the local net flux contribution to the global matrix is given by $-F_S + F_E$. Gathering coefficients of each ϕ_j, $j = 1,\ldots,4$ the net flux is written such that

$$-F_S + F_E = -\frac{1}{2}(\phi_1(T_{11} - (T_{11}+T_{22})\eta) - \phi_2((T_{11}+T_{22})(1-\eta) - T_{12}) + \phi_3(T_{22} - (T_{11}+T_{22})\eta) + \phi_4((T_{11}+T_{22})\eta - T_{12})). \tag{42}$$

Next the conditions for Eq. (34) to hold are tested. First conditions for non-positive off-diagonal coefficients are derived. The ϕ_4 coefficient is non-positive if

$$|T_{12}| \leqslant \eta(T_{11}+T_{22}) \tag{43}$$

and the coefficients of ϕ_1 and ϕ_3 are non-positive if

$$\eta(T_{11}+T_{22}) \leqslant \min(T_{11}, T_{22}). \tag{44}$$

Thus taking the inequalities together we obtain

$$|T_{12}| \leqslant \eta(T_{11}+T_{22}) \leqslant \min(T_{11}, T_{22}) \tag{45}$$

from which it follows that the diagonal coefficient of ϕ_2 is positive since $0 \leqslant \eta < \frac{1}{2}$. Finally since the positive coefficient of ϕ_2 is equal to the sum of absolute values of the off-diagonal coefficients, the latter inequality of Eq. (34) is confirmed. Strict inequality is obtained when a Dirichlet condition is imposed. We note that Eq. (45) is identical to Eq. (36) which also confirms the sufficient conditions for a single family of M-matrix full-tensor schemes, cf. [3]. The M-matrix conditions of Eq. (45) can also be seen to be sufficient by inspection of Table 2, where the left-hand inequality is sufficient for M_{13}, M_{15}, M_{17}, M_{19} to each be non-positive and the right-hand inequality is sufficient for M_{12}, M_{14}, M_{16}, M_{18} to each be non-positive and for diagonal dominance with $M_{11} > 0$. These conditions now establish the following theorem:

Conditional M-matrix: Any single parameter η—family of consistent locally conservative schemes on or within the 9-point stencil applied to a locally constant full-tensor field can only provide a conditional M-matrix subject to Eq. (45). Note: FPS is exact for piecewise linear and bilinear fields, since the pressure basis functions are piecewise bilinear.

For example, the inequality of Eq. (45) shows that if a locally constant full-tensor is present and the basic scheme is employed, i.e. $\eta = 0$ then the M-matrix condition is unconditionally violated. However, if $\eta \neq 0$, it is possible to still obtain an M-matrix provided that Eq. (45) is satisfied, which places clear limitations on the range of full-tensor coefficients permissible. Also since $\eta = 1/3$ corresponds the Galerkin finite element method [34] it follows that the well known Galerkin method is also subject to a conditional M-matrix. Examples will be presented in the results section.

7.4. Variable support reduction and 7-point schemes

As noted in [3], if we choose quadrature points with

$$\eta = |T_{12}|/(T_{11}+T_{22}) \tag{46}$$

then an M-matrix is obtained subject to a sufficient condition for ellipticity, i.e.

$$|T_{12}| \leqslant \min(T_{11}, T_{22}) \tag{47}$$

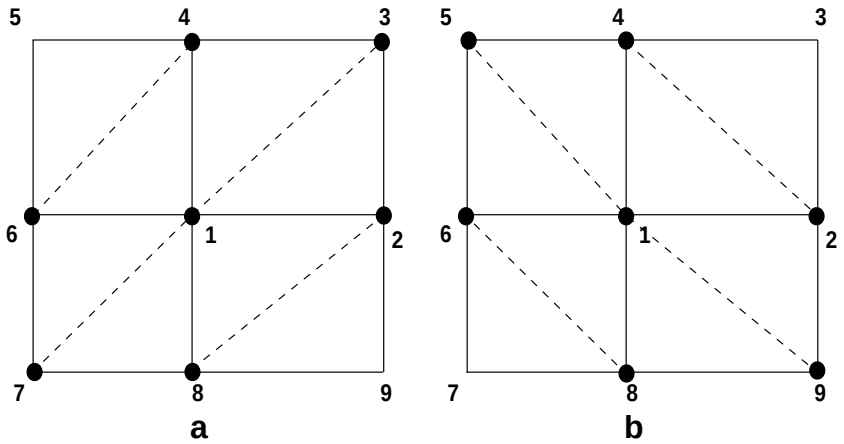

Fig. 9. (a) T_{12} positive over all contributing dual-cells-right inclined 7 pt scheme (solid nodes). (b) T_{12} negative over all contributing dual-cells-left inclined 7 pt scheme (solid nodes).

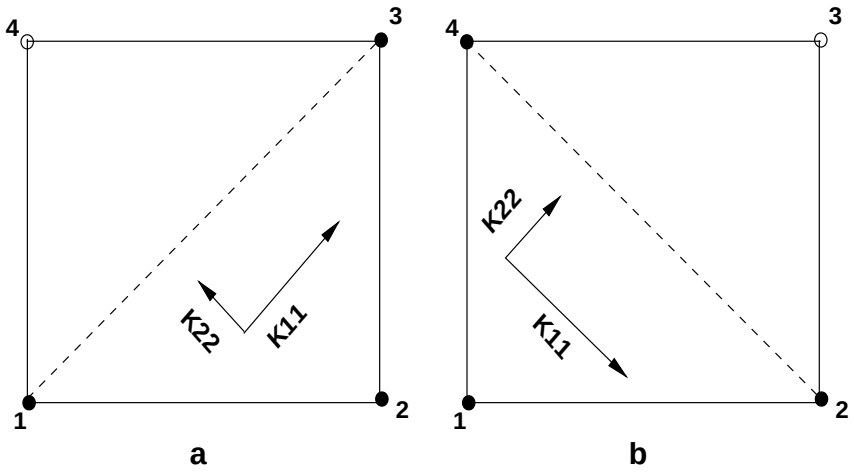

Fig. 10. (a) Net positive T_{12} over a dual-cell: Optimal support scheme for control-volume at 2 uses nodes 1, 2, 3 (b) Net negative T_{12} over a dual-cell: Optimal support scheme for control-volume at 1 uses nodes 4, 1, 2.

Table 4
Optimal support $\eta = |T_{12}|/(T_{11} + T_{22})$ (FPS) coefficients for constant tensor field

Integer coordinates	Coefficients	Full tensor
i, j	M_{11}	$2(T_{11} + T_{22}) - 2\|T_{12}\|$
$i + 1, j$	M_{12}	$-T_{11} + \|T_{12}\|$
$i + 1, j + 1$	M_{13}	$-\frac{1}{2}(\|T_{12}\| + T_{12})$
$i, j + 1$	M_{14}	$-T_{22} + \|T_{12}\|$
$i - 1, j + 1$	M_{15}	$-\frac{1}{2}(\|T_{12}\| - T_{12})$
$i - 1, j$	M_{16}	$-T_{11} + \|T_{12}\|$
$i - 1, j - 1$	M_{17}	$-\frac{1}{2}(\|T_{12}\| + T_{12})$
$i, j - 1$	M_{18}	$-T_{22} + \|T_{12}\|$
$i + 1, j - 1$	M_{19}	$-\frac{1}{2}(\|T_{12}\| - T_{12})$

giving the upper limit on the tensor cross-term. Upon examination of Eq. (42) we see that choosing the FPS (or equivalent CVFE) quadrature point of Eq. (46) naturally reduces the coefficient of local node 4 to zero if $T_{12} > 0$, Fig. 10a. This is also clear from the CVFE Table 2 centred on node 1. If the local tensor field has a positive cross-term for each contributing cell the net effect is to reduce a 9-point scheme to a 7-point (triangle) scheme with upward "+ve" support as indicated in Fig. 9(a), also by CVFE Table 2 (for a constant tensor) $M_{15} = M_{19} = 0$ while the other off-diagonals are non-positive subject to Eq. (47). Conversely a similar analysis for the net flux contribution at node 1 reveals that if $T_{12} < 0$ a downward "-ve" triangle support" is obtained Fig. 9(b), again this is also verified by inspection of the CVFE Table 2 where in this case $M_{13} = M_{17} = 0$ when Eq. (46) holds. We shall refer to Eq. (46) as the *optimal support condition*. We also note that Eq. (47) is consistent with the triangular grid M-matrix conditions presented in [5,6], and defines the M-matrix *upper limit* for the cross coefficient $|T_{12}|$.

In general the choice of quadrature defined by Eq. (46) leading to (*optimal support*) yields a scheme that will select a variable support Fig. 10(a) and (b) that favours the local tensor anisotropy orientation (sign of the cross-terms) and can vary between a 9-point scheme to a seven point scheme (on a structured grid) and maintain an M-matrix provided Eq. (47) holds. The general condition for 9-point schemes to reduce their support (seven point schemes of this type only result if cross terms are of the same sign for all contributing cells) depends upon η being chosen such that Eq. (46) holds. The resulting scheme with quadrature defined by Eq. (46) leading to *optimal support* is given in Table 4 for a spatially constant full-tensor coefficient field.

As can be seen from Table 4, the optimal support scheme relies upon exact algebraic cancelation for actual reduced support. Otherwise when coefficients vary over the sub-cells algebraic cancelation is unlikely, optimal support is then only achieved either by anisotropy angle favouring triangulation [33] or by special case construction according to anisotropy [41].

8. TPS versus FPS quadrature range

The key advantage of full pressure support (FPS) over the triangle pressure support (TPS) formulation becomes apparent when considering the range of validity of the quadrature points. The family of CVFE schemes which includes all spatially con-

stant full-tensor 9-point schemes and their subsets are well defined for $0 \leqslant \eta < \frac{1}{2}$, or alternatively in terms of the common parameterization q defined above, for $1 \geqslant q > 0$.

8.1. TPS

The TPS $\eta(q)$ has a non-linear variation with respect to q, c.f. Eq. (40) and Table 1. At the ends of the [0,1] q-interval for TPS

$$\begin{aligned} \eta(0) &= \frac{1}{4}(1+E), \\ \eta(1) &= \frac{1}{2}E \end{aligned} \tag{48}$$

which reveals that this scheme has a reduced quadrature range for the general case. From Eq. (40) $\mathrm{d}\eta/\mathrm{d}q \leqslant 0$ and it follows that $\eta(0)$ and $\eta(1)$ are the respective maximum and minimum values of η for TPS. For example if cross-terms vanish with $E = 0$ then the maximum range is $\eta(0) = \frac{1}{4}$, where as $\eta_{\mathrm{CVFE}} < \frac{1}{2}$. Thus the CVD TPS schemes do not include all possible 9-point schemes, allowing only half the range in the diagonal tensor case. Also for $E \neq 0$ the minimum end of the range below $E/2$ to ($\eta = 0$) is excluded.

If Eq. (47) holds, then it follows from the maximum and minimum values of η (Eq. (48)) that a TPS M-matrix scheme can be obtained and Eq. (46) can be employed to obtain optimal support for a limited range of tensor coefficients satisfying Eq. (47). However, in contrast to the FPS family, due to the limited quadrature range of TPS for full-tensors with strong anisotropy ratios where Eq. (47) is violated, the value of q required for Eq. (40) to equate to Eq. (46) is outside the quadrature range when the optimal quadrature point of Eq. (46) is less than the minimum TPS quadrature $\eta = E/2$. This occurs when

$$|T_{12}| > 2T_{11}T_{22}/(T_{11}+T_{22}). \tag{49}$$

The latter inequality holds in three test cases presented in the results section.

8.2. FPS

In contrast for CVD FPS the end interval values are from Eq. (41) and Table 3

$$\begin{aligned} \eta(0) &= \frac{1}{2}, \\ \eta(1) &= \frac{c}{2(1+pc-c)}ER, \end{aligned} \tag{50}$$

which recovers the upper bound of 1/2 for maximum quadrature range for a diagonal or full-tensor. However from Eq. (50) the lower bound $\eta(1)$ only tends to zero if the auxiliary control-volume size tends to zero, which occurs in the limit as $c \to 0$, showing the value of allowing the control-volume size to vary. Crucially the variation of FPS $\eta(q)$ is essentially linear in q for $1 \geqslant q > 0$ provided that c is sufficiently small. From Eq. (41) as $c \to 0$ then $\eta(q) \to (1-q)/2 = \tilde{\eta}/2$ yielding direct correspondence between FPS and the full family of CVFE schemes for spatially constant tensor coefficients, leading to a quadrature range that embraces all classical single parameter nine-node schemes.

We have already noted that Eq. (46) leads to a reduced support scheme, and in particular yields a 7-point scheme if all contributing cross-terms are of the same sign. In the general case Eq. (46) can be used to define $\eta(q)$ locally over each sub-cell cluster comprising a dual-cell, according to the local tensor variation. The local sign of the cross-terms over the dual-cell determines the ultimate support of the FPS scheme. Thus Eq. (46) yields an example of an FPS scheme that self adapts the support, in this case such that *optimal support* is naturally selected for any tensor, since by ellipticity $|T_{12}| / (T_{11} + T_{22}) \leqslant 1/2$. For small cross-terms, if $T_{12} \to 0$ the quadrature Eq. (46) defaults to zero yielding the basic diagonal-tensor 5-point operator.

Other M-matrix schemes that adapt the quadrature point according to the local tensor variation can also be defined by choosing other values of $\eta(q)$ that lie in the range defined by Eq. (45). For example choosing the right hand bound $\eta = \min(T_{11}, T_{22})/(T_{11} + T_{22})$ leads to another type of reduced support scheme (H/I support discussed below and see Appendix 2). Note here that the M-matrix conditions again reduce to Eq. (47) and $\eta \to 0$ as the anisotropy and/or grid aspect ratio increases.

In the general case when the tensor varies over the dual-cell Fig. 2 a locally upscaled tensor is used to determine the quadrature point for the dual-cell, so that the range defined by Eq. (45) and any consequent choice of $\eta(q)$ in the range will always be based on a locally upscaled average tensor, here local 2×2 renormalization of [36] is used to define the 2×2 sub-cell average tensor over the dual-cell. Consequently the optimal bound defined by Eq. (46) can only be defined with respect to the local mean tensor of the dual-cell and will not necessarily have exact *optimal support*. If Eq. (47) holds, then FPS may still have an M-matrix. If Eq. (47) is violated FPS does not have an M-matrix with respect to the mean tensor, but the *mean optimal* quadrature point can still be employed. The effects and practical implications of this are considered below in the section on quasi-positive schemes.

8.3. M-matrix diagrams

Here we present illustrative M-matrix diagrams for FPS in the (x, y) plane where we let $T_{22} = \min(T_{11}, T_{22})$ and define $x = |T_{12}|/T_{11}$, $y = T_{22}/T_{11}$, so that $0 \leqslant x, y \leqslant 1$. Due to the non-linear nature of the TPS quadrature point of Eq. (40) with respect to x, y there is no linear correspondence between TPS and FPS in the (x, y) plane for a given value of q. Also, while any TPS η quadrature point belongs to FPS, the converse is not true because FPS has the larger quadrature range. FPS M-matrix diagrams are shown for $\eta = (0.25, 1/3, 0.45)$ in Fig. 11 and for the optimal point of Eq. (46) where $\eta = x/(1 + y)$ in Fig. 15a (corresponding to $y \geqslant x$). The diagrams are composed of the bounds of the inequality conditions of Eq. (45).

9. Decoupled approximation

The quadrature point $\eta = 1/2$ is a singular point for the above CVFE, FPS and TPS approximations (see Tables 5 and 6). Again as a consequence of the above relationships of Eqs. (40) and (41) for a spatially constant tenor field, we need only substitute $\eta = 1/2$ in the CVFE approximation to see the effect. Referring to Table 2 we obtain the scheme in Table 5.

We note that the resulting discretization permits the *checker board* solution, Table 6.

The solution is strongly oscillatory and decoupled, Fig. 12. This helps to explain the extreme sensitivity of the TPS scheme, where for a highly anisotropic full-tensor, the ellipticity measure $E = T_{12}^2/(T_{11}T_{22})$ tends to unity, for the example (below) $E = 0.99776$, by Eq. (48) it follows that $\eta(TPS) \to 1/2$ for any value of q, resulting in an oscillatory decoupled solution. Therefore for a highly anisotropic full-tensor violating the M-matrix condition, we may regard the TPS family as belonging to the interval

$$1/2 - \epsilon_{\mathrm{TPS}} < \eta \leqslant 1/2, \tag{51}$$

where $\eta_{\mathrm{DC}} = 1/2 - \epsilon_{\mathrm{TPS}}$ defines a cut-off limit above which decoupling takes place (suffix DC denotes decoupled). The precise cut-off limit is at present undetermined, but a first estimate is obtained from the minimum of the TPS range with $1/2 - \epsilon_{\mathrm{TPS}} \sim E/2$.

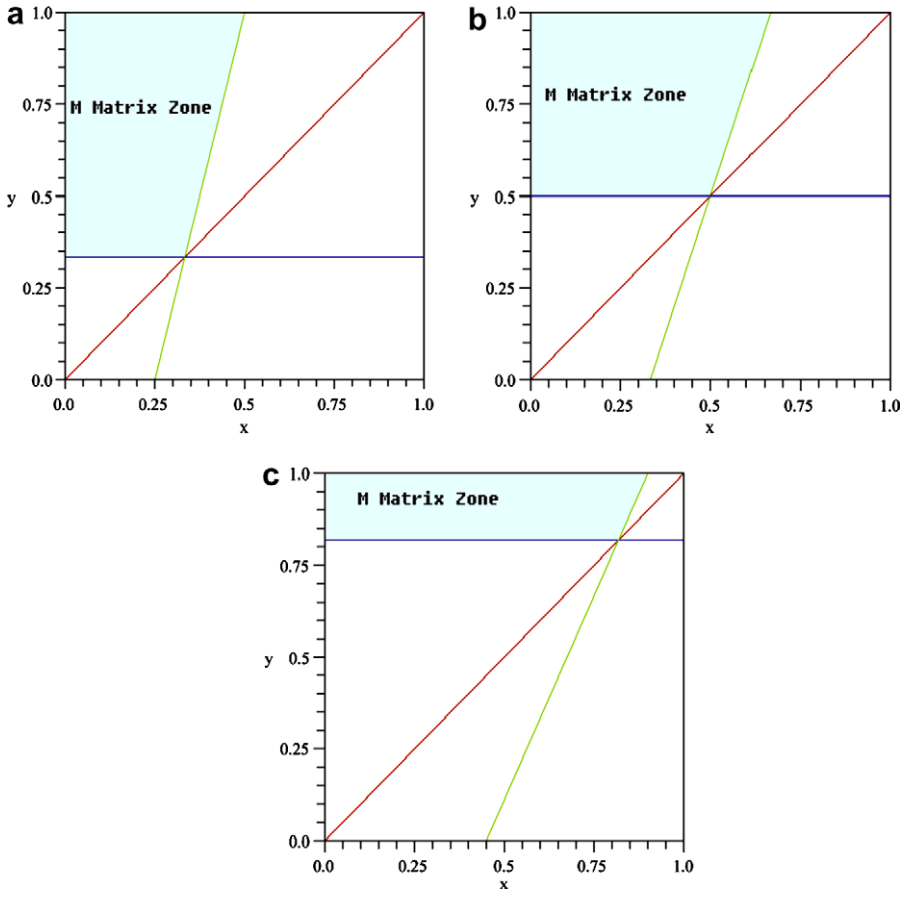

Fig. 11. M-matrix zones for examples of η: (a) $\eta = \frac{1}{4}$. (b) $\eta = \frac{1}{3}$. (c) $\eta = 0.45$.

Table 5
CVFE coefficients for constant tensor field: $\eta = 1/2$

Integer coordinates	Coefficients	Full tensor
i, j	M_{11}	$(T_{11} + T_{22})$
$i+1, j$	M_{12}	$\frac{1}{2}(T_{22} - T_{11})$
$i+1, j+1$	M_{13}	$-\frac{1}{4}(T_{11} + T_{22}) - \frac{1}{2}T_{12}$
$i, j+1$	M_{14}	$\frac{1}{2}(T_{11} - T_{22})$
$i-1, j+1$	M_{15}	$-\frac{1}{4}(T_{11} + T_{22}) + \frac{1}{2}T_{12}$
$i-1, j$	M_{16}	$\frac{1}{2}(T_{22} - T_{11})$
$i-1, j-1$	M_{17}	$-\frac{1}{4}(T_{11} + T_{22}) - \frac{1}{2}T_{12}$
$i, j-1$	M_{18}	$\frac{1}{2}(T_{11} - T_{22})$
$i+1, j-1$	M_{19}	$-\frac{1}{4}(T_{11} + T_{22}) + \frac{1}{2}T_{12}$

Table 6
CVFE decoupled solution at $\eta = 1/2$

Integer coordinates	ϕ
i, j	C
$i+1, j$	$-C$
$i+1, j+1$	C
$i, j+1$	$-C$
$i-1, j+1$	C
$i-1, j$	$-C$
$i-1, j-1$	C
$i, j-1$	$-C$
$i+1, j-1$	C

C is an arbitrary constant.

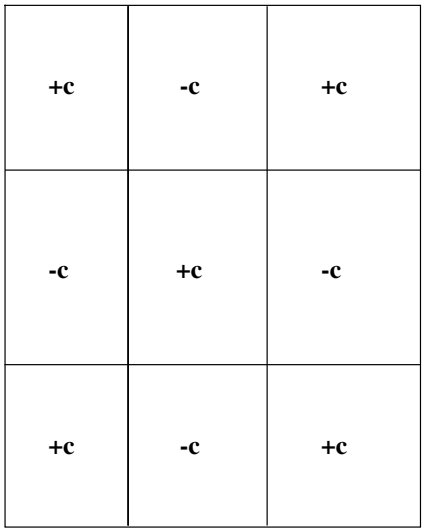

Fig. 12. Decoupled solution.

10. Quasi-positive QM-matrices

The practical effects of this comparison in terms of benefit and validity of quadrature is seen in the results section. First we return to the case of a spatially constant tensor. If the optimal quadrature point of Eq. (46) is chosen when the system has no M-matrix (and the matrix is not monotone), i.e. when $|T_{1,2}| > \min(T_{1,1}, T_{2,2})$, then inspection of Table 4 shows that the matrix coefficients $M_{13}, M_{15}, M_{17}, M_{19}$ still remain non-positive. For ellipticity we must have $|T_{12}| \leqslant \max(T_{11}, T_{22})$ so that either

M_{12} and M_{16} or M_{14} and M_{18} are non-positive. Without loss of generality, suppose that $T_{11} = \max(T_{11}, T_{22})$, then under the assumption of violation of Eq. (47) M_{12} and M_{16} will be non-positive and M_{14} and M_{18} will be positive. Therefore in this case, only two off-diagonal coefficients violate the M-matrix conditions, which by symmetry of the matrix is the least number possible.

Next we identify other quadrature points that lead to matrices with the minimum of only one unique positive off-diagonal coefficient that violates the M-matrix conditions. Note; in this case there are two offending off-diagonal coefficients by symmetry. We shall refer to the resulting matrices as Quasi-Positive M-matrices or QM-matrices (the name is also motivated in part by the essentially non-oscillatory solutions obtained with the schemes). By symmetry we only have to consider the four coefficients M_{12}, M_{13}, M_{14}, M_{15}.

Returning to Table 2, we now consider general η where $\eta < 1/2$ and suppose $T_{11} = \max(T_{11}, T_{22})$ with $T_{12} > 0$, it follows that M_{12} and M_{13} are non-positive. Depending on the size of η it follows that M_{14} and M_{15} can change sign.

Case 1.0: Crucially if $M_{14} \leqslant 0$ it follows that $\eta \leqslant T_{22}/(T_{11} + T_{22})$, by the above supposition $|T_{1,2}| = T_{1,2} > T_{22}$ and it follows that $M_{15} > 0$ and by symmetry $M_{19} > 0$.

Case 2.0: Conversely if we assume $M_{15} \leqslant 0$, then $\eta \geqslant |T_{1,2}|/(T_{11} + T_{22})$ and by the above supposition $M_{14} > 0$ and by symmetry $M_{18} > 0$.

By matrix symmetry it follows that in both cases 1 and 2, we obtain further QM-matrices where only 2 coefficients violate the M-matrix conditions over the two intervals

$$\begin{aligned} &0 \leqslant \eta \leqslant T_{22}/(T_{11} + T_{22}) \\ &|T_{1,2}|/(T_{11} + T_{22}) \leqslant \eta < 1/2 - \epsilon_{\mathrm{TPS}} \end{aligned} \tag{52}$$

and where solutions are essentially free of spurious oscillations. The upper bound of $1/2 - \epsilon_{\mathrm{TPS}}$ in the second interval ensures that η never enters the decoupled zone of Eq. (51), where the method can produce decoupled oscillatory solutions as shown above. We note by inspection of M_{14} and M_{15} in Table 2, referring to the respective intervals of Eq. (52), as η decreases over the first interval and as η increases over the second interval the offending positive coefficient increases in size in each case. This shows that the schemes defined by the quadrature points

$$\eta = \min(T_{11}, T_{22})/(T_{11} + T_{22}), \tag{53}$$

$$\eta = |T_{1,2}|/(T_{11} + T_{22}) \tag{54}$$

are both optimal over their respective intervals in the sense that they lead to matrices that are both the closest matrices to M-matrices in pattern, with the minimum number (two due to symmetry) of off-diagonal coefficients that violate the M-matrix conditions, and that the violating coefficients are minimized in magnitude at these points, subject to the constraint that only one of the four unique off-diagonal coefficients is positive.

We shall denote the optimal quadrature points of Eqs. (53) and (54) by η_{HI} and η_{OS} respectively. The case $\eta_{HI} = \min(T_{11}, T_{22})/(T_{11} + T_{22})$ leads to a reduced support scheme with H support when $T_{22} = \min(T_{11}, T_{22})$ (with coefficients given in Appendix 2) as indicated in Fig. 13a and alternatively if $T_{11} = \min(T_{11}, T_{22})$ we obtain a scheme with I support as shown in Fig. 13b, hence the general index HI. The optimal support (OS) point $\eta_{\mathrm{OS}} = |T_{1,2}|/(T_{11} + T_{22})$ is more attractive since this leads to optimal support that favours the anisotropy of the problem, as discussed earlier and is found to yield improved results, as presented below.

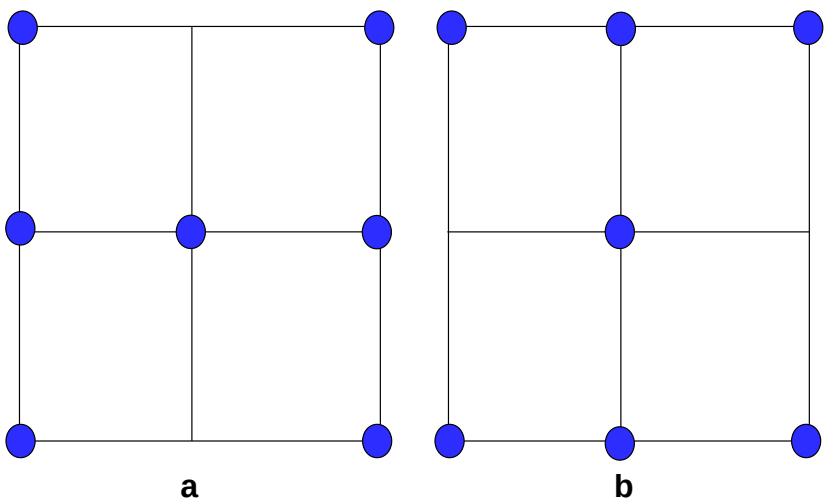

Fig. 13. Stencil of H/I scheme. (a) H scheme (b) I scheme.

Returning to the case where $T_{22} = \min(T_{11}, T_{22})$, the interval

$$T_{22}/(T_{11}+T_{22}) < \eta < T_{12}/(T_{11}+T_{22}) \tag{55}$$

connects the above minimum positive coefficient intervals of Eq. (52). In this case two unique off-diagonal coefficients M_{14} and M_{15} are found to be positive. It is interesting to note that this interval is precisely the reverse of the M-matrix interval of Eq. (45) and now contains the maximum number of offending coefficients, i.e. four by symmetry. However the four positive coefficients are always bounded above by the maximum of the coefficients at the optimal points.

We next plot the coefficients M_{12}, M_{13}, M_{14}, M_{15} against η in Fig. 14, for an example where $T_{11} = \max(T_{11}, T_{22})$ and $T_{12} > 0$. In this example

$$\mathbf{T} = [2464.360020, 1148.683643, 1148.683643, 536.6399794].$$

The intervals in Fig. 14 are (a) the first of Eq. (52), i.e. $[0, \eta_{HI}]$, (b) Eq. (55), i.e. $[\eta_{HI}, \eta_{OS}]$, (c) second of Eq. (52), i.e. $[\eta_{OS}, \eta_{DC}]$, (d) the decoupled (TPS) interval $[\eta_{DC}, 1/2]$. The QM-matrices complement the M-matrices so that the entire elliptic region is covered as indicated in Fig. 15b.

A further consequence of this analysis is that for η belonging to the above intervals (a)–(c) (and always away from the singular point), when not equal to one of the optimal points, the QM-matrix schemes will again have up to 9-points in sup-

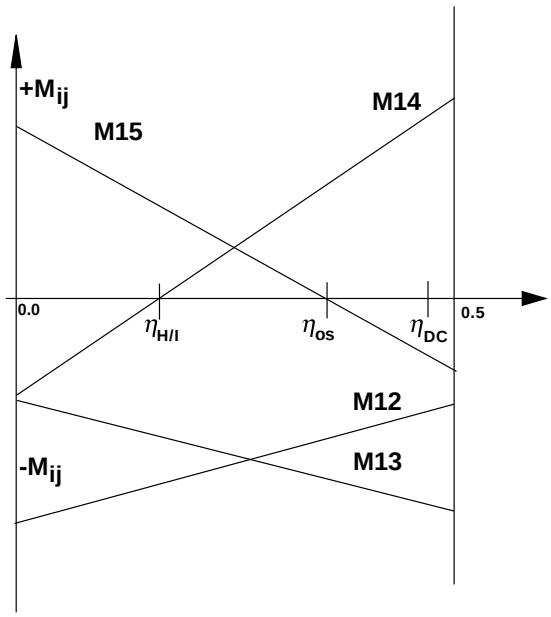

Fig. 14. Unique coefficients M12, M13, M14, M15 versus η (quadrature range).

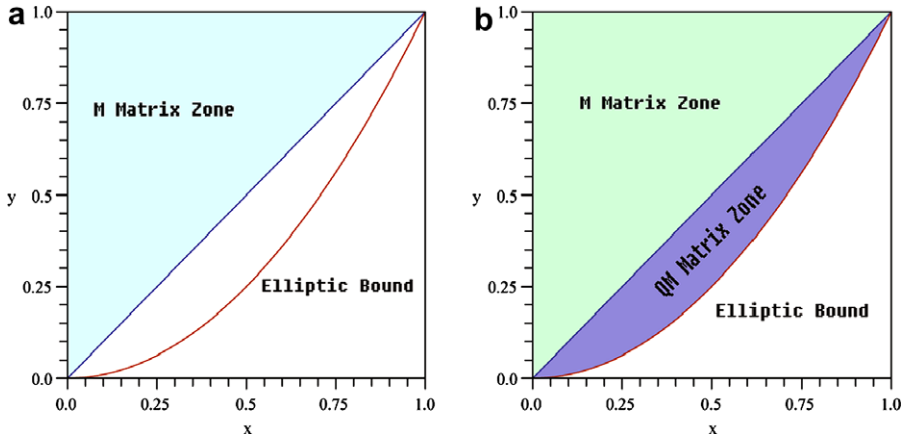

Fig. 15. M-matrix zone and QM-matrix zone for optimal support FPS scheme. (a) Optimal support M-matrix zone (b) QM-matrix zone.

port. This is an important observation when applying the method to heterogeneous cases where a locally upscaled tensor is used to define the unique η optimal quadrature point over a dual-cell as discussed above. Note that the upscaled tensor is only used to define the quadrature, once the quadrature is defined, the flux-continuous method is then used to solve the original problem with the original permeability field. For general permeability variation the resulting value of η is unlikely to lead to *exact* optimal support, but can still improve solution resolution. Numerical pressure solutions are compared for a range of quadrature points spanning the quadrature interval and show that well resolved solutions are obtained within a range of 15% of the optimal point.

Finally we again emphasize that the above analysis is for constant coefficients. The discrete matrix will not necessarily be symmetric in the general case, e.g., for general quadrilateral cells with a physical space formulation (where exact geometry is maintained in the finite-volume flux) and the coefficients will not take such a simple form. However, the above analysis still provides an important guide in terms of discretization effects.

11. Numerical results

A comparison is now presented between the new full pressure support formulation and earlier triangular pressure support formulation. As with the TPS family, the new FPS family of schemes are exact for piecewise linear test cases with jumps in full-tensor permeability. However unlike TPS, the FPS formulation is also exact for piecewise bilinear pressure fields with jumps in full-tensor permeability, consistent with the FPS sub-cell bilinear basis functions. Convergence behaviour has been found to match that of the TPS schemes for earlier lower anisotropy test cases, an example of convergence is given in case 1. Cases 2, 3 and 4 below demonstrate the advantages of the new methods in terms of preventing spurious oscillations.

11.0.1. CASE 1: piecewise quadratic test case

The first case is from [3]. In this case the pressure field is varying piecewise quadratically over the domain shown in Fig. 16. The domain discontinuity is aligned along the line $x = 1/2$, and the analytical solution is given by

$$
\begin{aligned}
&\phi(x,y) = \begin{cases} c_l x^2 + d_l y^2, & x < 1/2, \\ a_r + b_r x + c_r x^2 + d_r y^2, & x \geqslant 1/2, \end{cases} \\
&K = \begin{cases} \begin{pmatrix} 50 & 0 \\ 0 & 1 \end{pmatrix}, & x < 1/2, \\ \begin{pmatrix} 1 & 0 \\ 0 & 10 \end{pmatrix}, & x \geqslant 1/2, \end{cases} \\
&\alpha = K_{11}|_r / K_{11}|_l, \\
&\beta = K_{22}|_l / K_{22}|_l, \\
&a_r = 1, \\
&f = 4a_r/((\alpha-2)\beta+1), \\
&b_r = (\beta-1)f, \\
&c_r = f, \\
&d_r = -c_r K_{11}|_r / K_{22}|_r, \\
&c_l = \alpha\beta c_r, \\
&d_l = d_r.
\end{aligned}
\tag{56}
$$

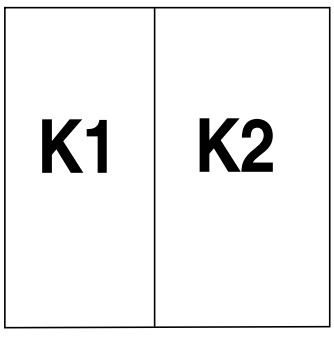

Fig. 16. Two sub-domains with discontinuous permeability.

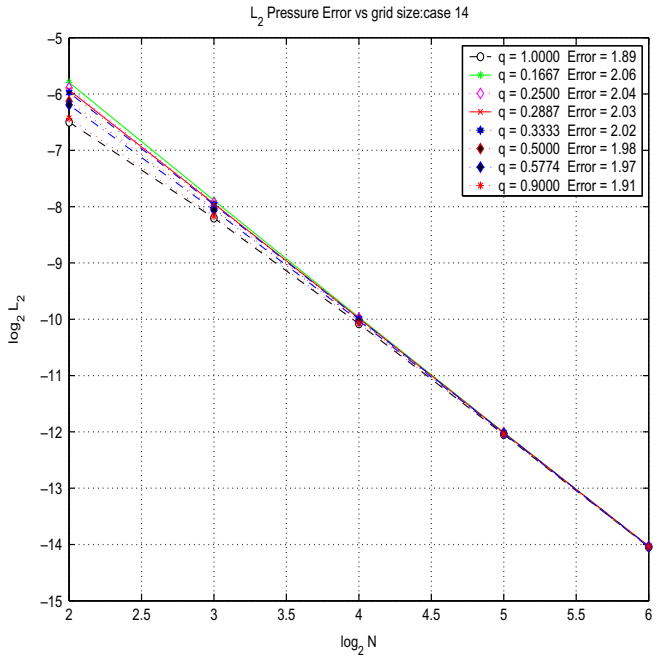

Fig. 17. L_2 Convergence rates for pressure, quadratic case-for a range of q.

Dirichlet boundary conditions are imposed, permeability is discontinuous across the line $x = 1/2$. Convergence rates for FPS are shown in Fig. 17. In this case $q = 0.1667$ gives the best convergence rate.

11.0.2. Optimal convergence

We also note that convergence tests reported in [41] indicate that their scheme yields optimal convergence for high anisotropy on distorted meshes. We have also observed this type of convergence behaviour on a similar problem using our optimal support quadrature point.

11.0.3. Case 2: planar full-tensor field

The second case involves a uniform anisotropic domain with a Green's function (point source) in the middle of the domain and with Dirichlet boundary pressure data defined by the Green's function.

The full-tensor is given by

$$\mathbf{K} = [2464.360020, 1148.683643, 1148.683643, 536.6399794] \tag{57}$$

with high anisotropy ratio 3000:1 and grid *non-aligned* with the principal axes, which are oriented at an angle of 25 degrees to the computational grid, leading to a full-tensor. The full-tensor field violates the inequality of Eq. (47) so that no 9-point scheme or subset scheme can possess an M-matrix in this case.

The first result involves using the TPS 9-point scheme with $q = 1$ on a 64×64 grid. The TPS numerical pressure solution is shown in Figs. 18(a) and 19(a) with visible strong spurious oscillations. We note that the condition of Eq. (46) could not be satisfied by the TPS scheme due to the limited quadrature range.

The family of FPS schemes are investigated here. The quadrature points that have been tested are given below

$$\eta = [0, 1/6, \eta_{H/I}, 1/4, 1/3, \eta_{OS} - \varepsilon, \eta_{OS}, \eta_{OS} + \varepsilon, 0.45], \tag{58}$$

where $\eta_{H/I}$, η_{OS} correspond to the two optimal QM-matrix schemes, here ε is defined by 15% of optimal support quadrature η_{OS}.

Results are shown for a 64×64 grid in Figs. 18 and 19. The solution resolution is seen to sharpen gradually from $\eta = 0$ to $\eta = 0.45$. In this case the solution in the range $\eta_{H/I}$ is found to be of a slightly more diffuse and smoother nature. At $\eta = 0.25$ the mid-point of the quadrature range, which would correspond with the scheme of [38], the solution is of medium resolution, but also indicates the formation of a trough either side of the peak. Since the tensor is spatially constant throughout the field the FPS family coincides with the CVFE family. Note in this constant coefficient case $\eta = 1/3$ corresponds to the Galerkin finite element method and $\eta = 1/6$ corresponds with the sixth-order accurate Laplacian operator when the tensor is diagonal

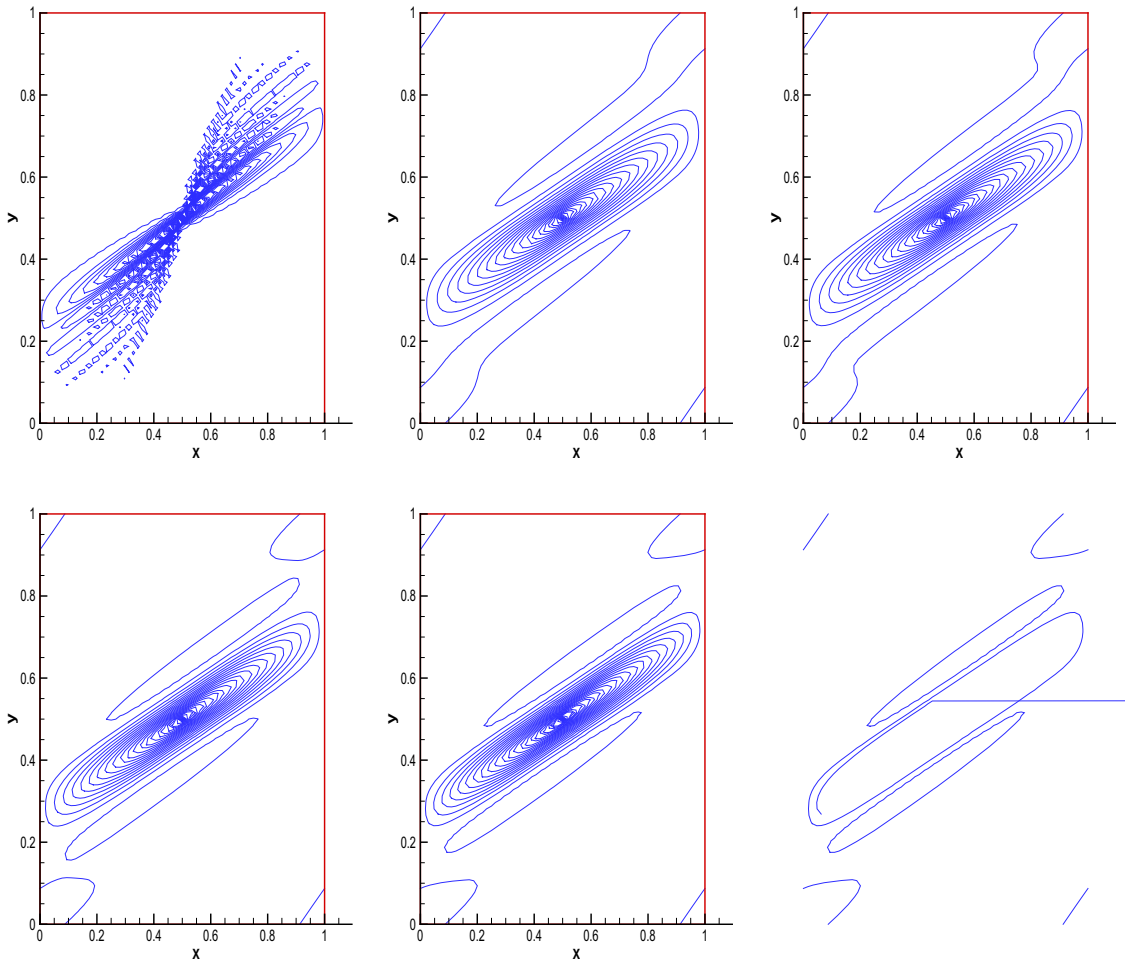

isotropic [34]. For $\eta = \eta_{OS}$ FPS has an angled 7-point approximation according to local orientation of the full-tensor field. Although a trough now forms either side of the peak, the numerical pressure solutions of Figs. 18 and 19 from (d) to (h) are otherwise of improved resolution and practically oscillation free for the entire quadrature of Eq. (58). The solutions corresponding to the interval $[\eta_{OS} - \varepsilon, \eta_{OS} + \varepsilon]$ (e) to (g) are seen to have quite comparable resolution.

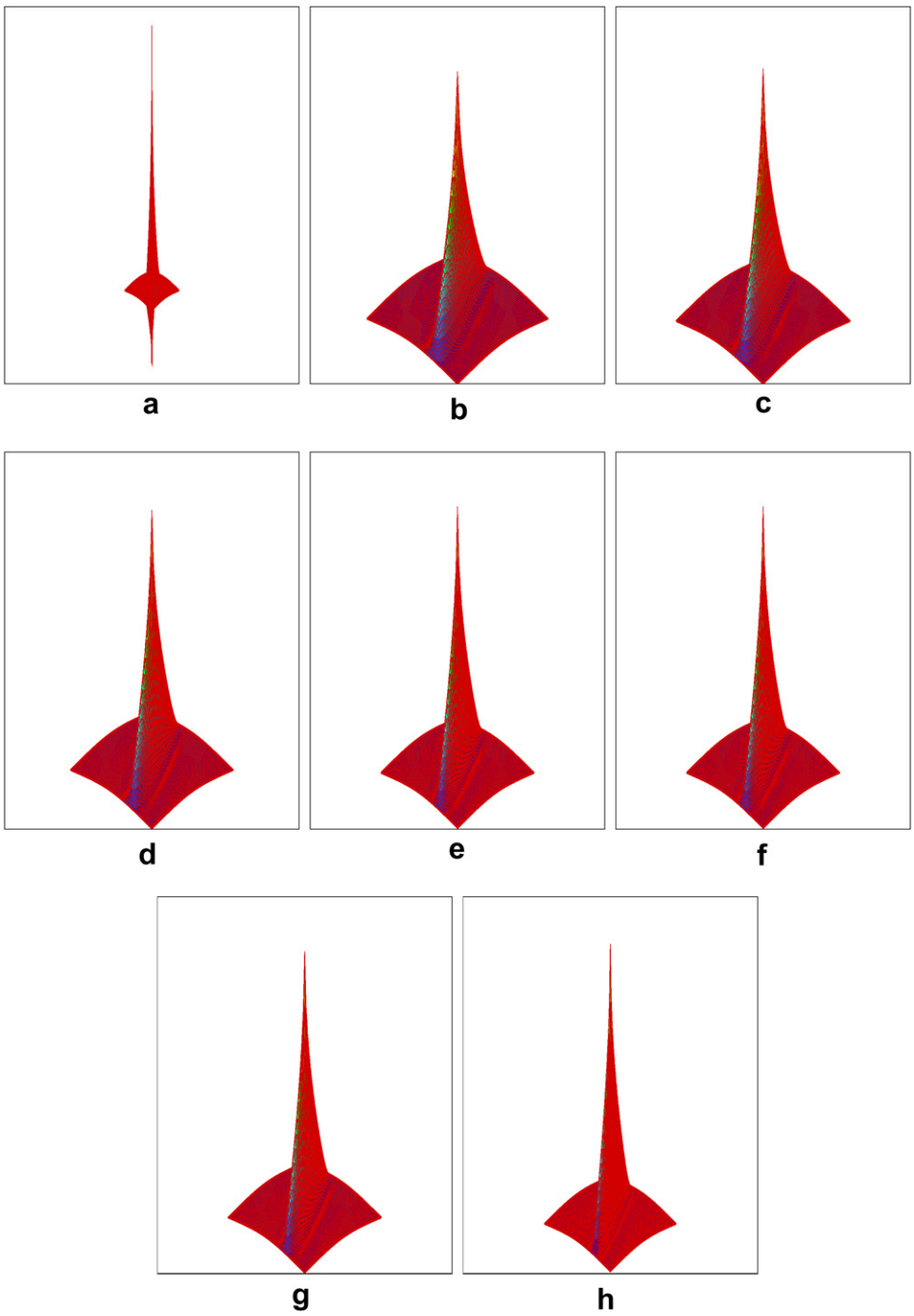

Fig. 19. Case 2: Iso-surface plots for homogeneous full-tensor case. (a) TPS $q = 1$. (b) FPS H scheme. (c) FPS $\eta = 0.25$. (d) FPS $\eta = \frac{1}{3}$. (e) FPS $\eta = \eta_{OS} - 15\%$. (f) FPS $\eta = \eta_{OS}$. (g) FPS $\eta = \eta_{OS} + 15\%$. (h) FPS $\eta = 0.45$.

11.0.4. Case 3: Strong discontinuous full-tensor (zigzag) field

In this case the boundary conditions for the unit domain involve a vertical line source placed across the middle of the second section for ($x = 0.5$, $0.25 \leqslant y \leqslant 0.75$) together with zero pressure prescribed on all boundary walls. The permeability tensor changes direction in anisotropy at one third and two thirds the way across the domain. The discontinuous full-tensor permeability field is defined below in sections varying from

$$\mathbf{K} = [2464.360020, +1148.683643, +1148.683643, 536.6399794]$$

to second section with

$$\mathbf{K} = [2464.360020, -1148.683643, -1148.683643, 536.6399794]$$

and third section with

$$\mathbf{K} = [2464.360020, +1148.683643, +1148.683643, 536.6399794]$$

as indicated in Fig. 20, at each section the principal axes are oriented at an angle of 25 degrees, (i.e. plus, minus, plus 25 degrees) to the computational grid. The tensor again has a principal anisotropy ratio of 3000:1, violating the *M*-matrix condition, Eq. (47) in each section. A 64×64 grid is employed for the computations.

Results are presented for the TPS scheme with $q = 1$. Figs. 21(a) and 22(a) for a 64×64 grid, again the condition of Eq. (46) could not be satisfied by the TPS scheme due to the smaller quadrature range (the cross-term is greater than the harmonic average of the diagonals, i.e. Eq. (49) holds in this case). There are very strong oscillations in the solution showing clear violation of the maximum principle as expected from the *M*-matrix analysis.

We now compare with the FPS scheme for the above range of quadrature points in case 2. A locally upscaled tensor is used to define the quadrature over the dual-cell, which yields a mean tensor for regions where permeability varies, in this case along the sub-domain boundaries where permeability is discontinuous.

We begin with the optimal scheme quadrature point defined by Eq. (46). In this case away from the discontinuities the support of the scheme reduces such that the scheme fulfills the *optimal support condition*. Thus away from the discontinuities this particular FPS scheme essentially leads to an angled approximation according to local orientation of the full-tensor field, the results are shown in Figs. 21(f) and 22(f). While oscillations are present for some quadrature points, they are seen to be considerably reduced compared to TPS and the solution is well resolved. Thus the FPS formulation yields almost oscillation free results for both planar and discontinuous full-tensor permeability fields.

In general, the solution resolution is seen to sharpen from $\eta = 0$ to $\eta = 0.45$, Figs. 21 and 22. Here solutions are seen to have quite comparable resolution in the interval $[1/3, \eta_{OS} + \varepsilon]$

11.0.5. Case 4: Strong discontinuous full-tensor 2 × 2 domain

In this case the boundary conditions involve a source and sink located at diagonally opposite points in the field (source lower left $\mathbf{r} = (0.25, 0.25)$ and zero pressure prescribed on the boundary walls. The permeability tensor changes direction in anisotropy over each quarter of the domain. With reference to sub-domains 1–4, the full-tensor field is defined by

$$\mathbf{K} = [2464.360020, +1148.683643, +1148.683643, 536.6399794]$$

in 1,

$$\mathbf{K} = [2464.360020, -1148.683643, -1148.683643, 536.6399794]$$

in 2,

$$\mathbf{K} = [2464.360020, +1148.683643, +1148.683643, 536.6399794]$$

in 3

$$\mathbf{K} = [2464.360020, -1148.683643, -1148.683643, 536.6399794]$$

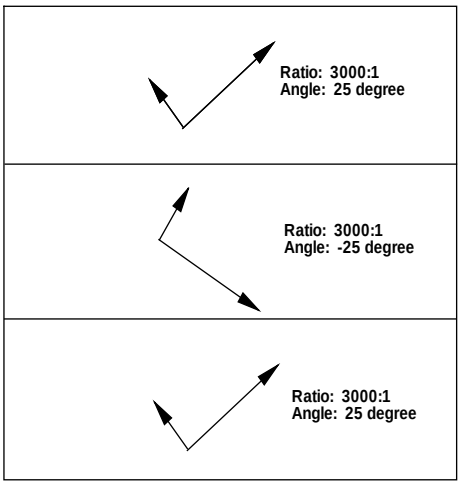

Fig. 20. Case 3: Principal axes of permeability in three sub-domains.

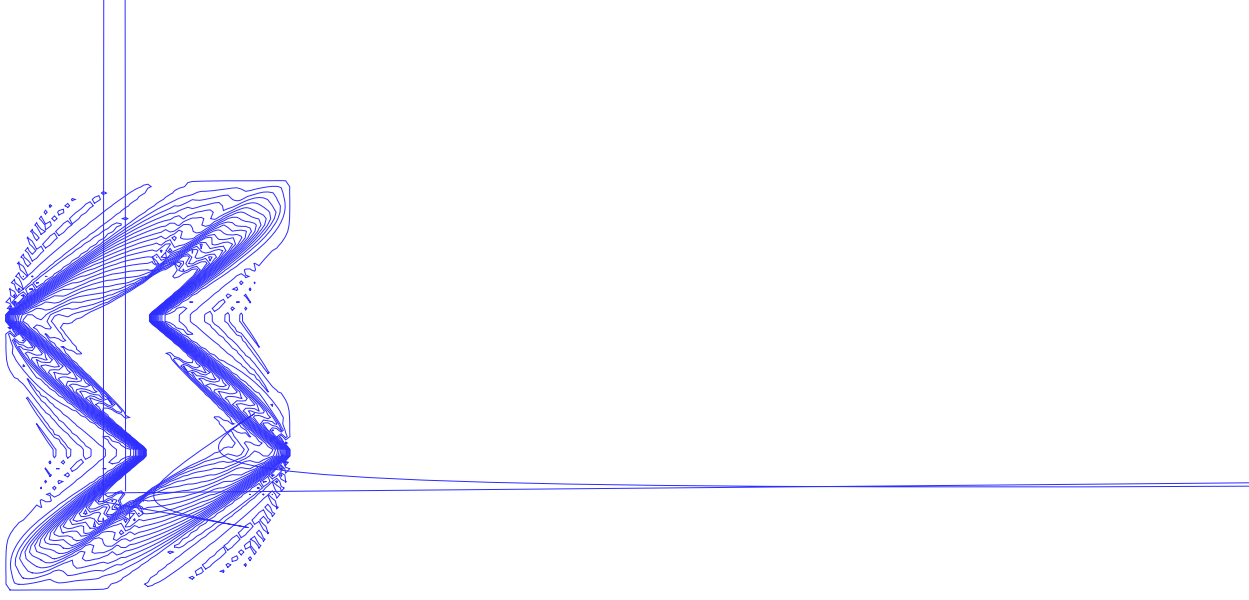

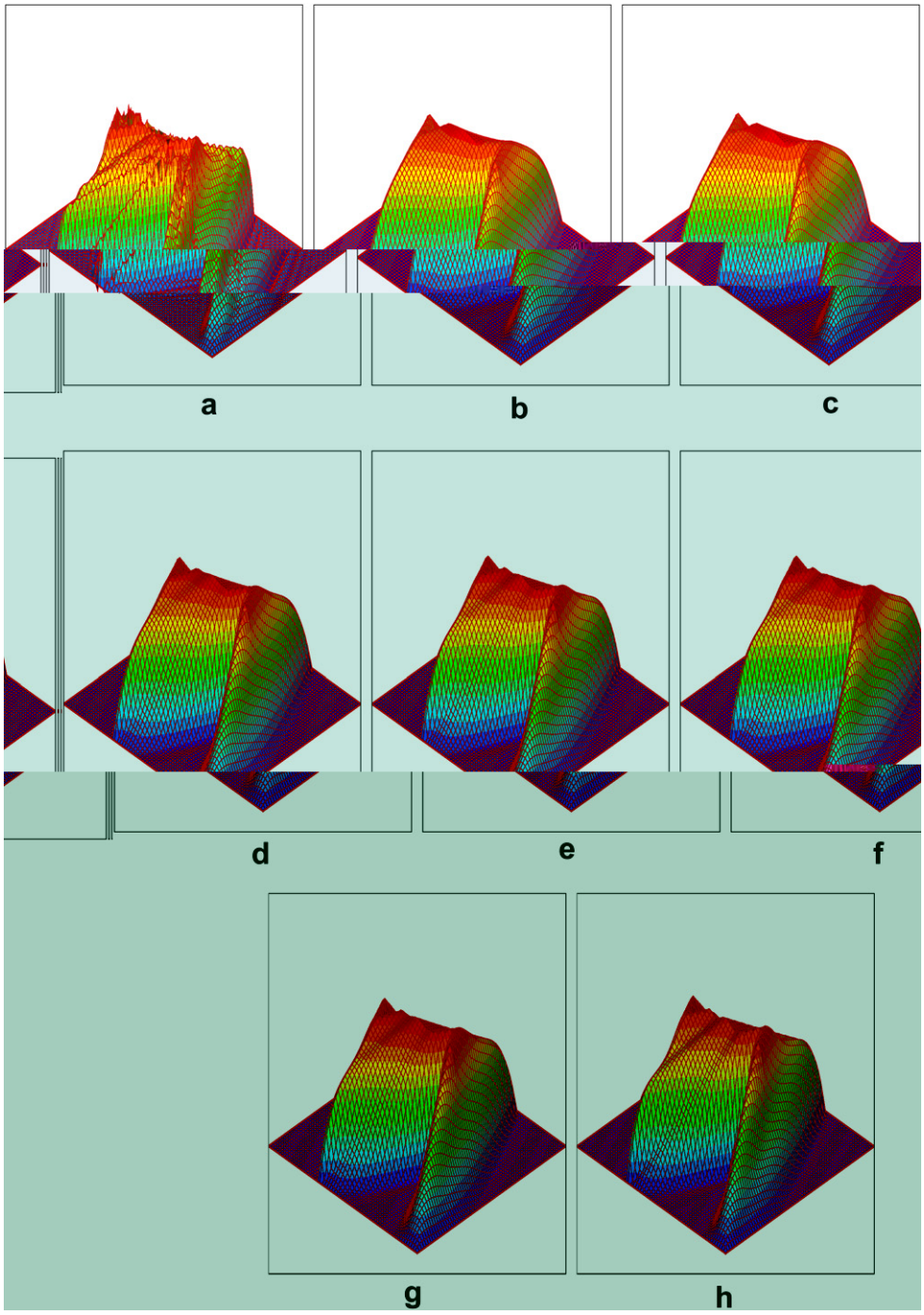

Fig. 22. Case 3: Iso-surface plot, 3 sub-domains. (a) TPS $q = 1$. (b) FPS H scheme. (c) FPS $\eta = 0.25$. (d) FPS $\eta = \frac{1}{3}$. (e) FPS $\eta = \eta_{OS} - 15\%$. (f) FPS $\eta = \eta_{OS}$. (g) FPS $\eta = \eta_{OS} + 15\%$. (h) FPS $\eta = 0.45$.

in 4, as indicated in Fig. 23. In each sub-domain the principal axes are oriented at an angle of +25 or −25 degrees, to the computational grid as indicated in Fig. 23. As before the tensor has a principal anisotropy ratio of 3000:1, and the elliptic tensor violates the condition for an M-matrix. A 64×64 grid is employed for the comparison.

Results from the TPS scheme with $q = 1$ Figs. 24(a) and 25(a) for a 64×64 grid, indicate the decoupling effect due to the small quadrature range at the upper end of the quadrature interval. Again there are very strong oscillations in the solution showing clear violation of the maximum principle.

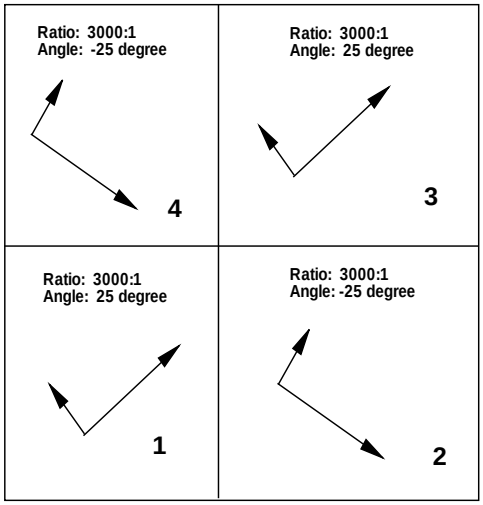

Fig. 23. Case 4: 2×2 sub-domains with local tensor principal axes orientations.

We next compare with the family of FPS schemes for the above range of quadrature points. This case leads to similar conclusions to the previous test. As in the previous case a locally upscaled tensor is used to define the quadrature over the dual-cell, which yields a mean tensor for regions where permeability varies, along the sub-domain boundaries where permeability is discontinuous.

For the optimal scheme quadrature point defined by Eq. (46), away from the discontinuities the support of the scheme reduces such that the scheme fulfills the *optimal support condition* with an angled approximation according to the local sign of cross-terms of the full-tensor field. The optimal quadrature point is based on a local mean tensor where permeability varies. Results are shown in Figs. 24 and 25.

In general, the solution resolution consistently sharpens from $\eta = 0$ to $\eta = 0.45$. Oscillations are not detected for some quadrature points. Here solutions are seen to have quite comparable resolution and be particularly well resolved for η in the interval [1/3,0.45], Figs. 24 and 25.

12. Conclusions

A new family of locally conservative flux-continuous, finite-volume schemes is presented for solving the general tensor pressure equation. The new family of schemes have full pressure continuity imposed across control-volume faces, in contrast to the earlier families of flux-continuous schemes, which are point-wise continuous in pressure and flux.

The new family of schemes offers maximum flexibility in range of quadrature. The permissible quadrature range of the earlier point-wise schemes is shown to be half that of the full continuity schemes for a diagonal tensor. When applying both the point-wise continuous schemes and full pressure continuity schemes to full-tensor fields with high anisotropy ratios, the schemes can fail to satisfy the maximum principle. For strong full-tensor anisotropy, the point-wise TPS schemes are shown to have quadrature points that lie within a small neighbourhood of the singular decoupled end point of the quadrature interval, leading to strong spurious oscillations in the solution.

The family of FPS schemes are shown to be symmetric positive definite for a spatially constant full elliptic tensor. Constant coefficient *M*-matrix analysis of the general family of full-tensor schemes define tensor-coefficient dependent quadrature interval limits for obtaining locally bounded solutions. When the governing conditions are satisfied the discrete pressure field is free of spurious oscillations. An *optimal support condition* is identified from the *M*-matrix analysis, via a bounding quadrature point that defines the upper limit on the tensor cross-term.

The new family of schemes are tested on a range of problems involving strong full-tensor anisotropy where both *M*-matrix and monotone matrix conditions are violated. Results are presented for a range of quadrature points belonging to the new family and show that the occurrence of spurious oscillations in the discrete pressure field is minimal provided the quadrature point lies outside of the neighbourhood of the point-wise continuity schemes which are essentially decoupled in this case. Analysis of the non-monotone case leads to the introduction of quasi-positive QM-matrices. The optimal support quadrature point is also shown to be optimal with respect to a QM-matrix.

The new full pressure support schemes are shown to share the full CVFE quadrature range for spatially constant tensor coefficients. The optimal support quadrature point is shown to lie within the quadrature range of the full pressure support scheme for all elliptic tensors. For regions where the tensor is spatially constant, the optimal support quadrature point yields

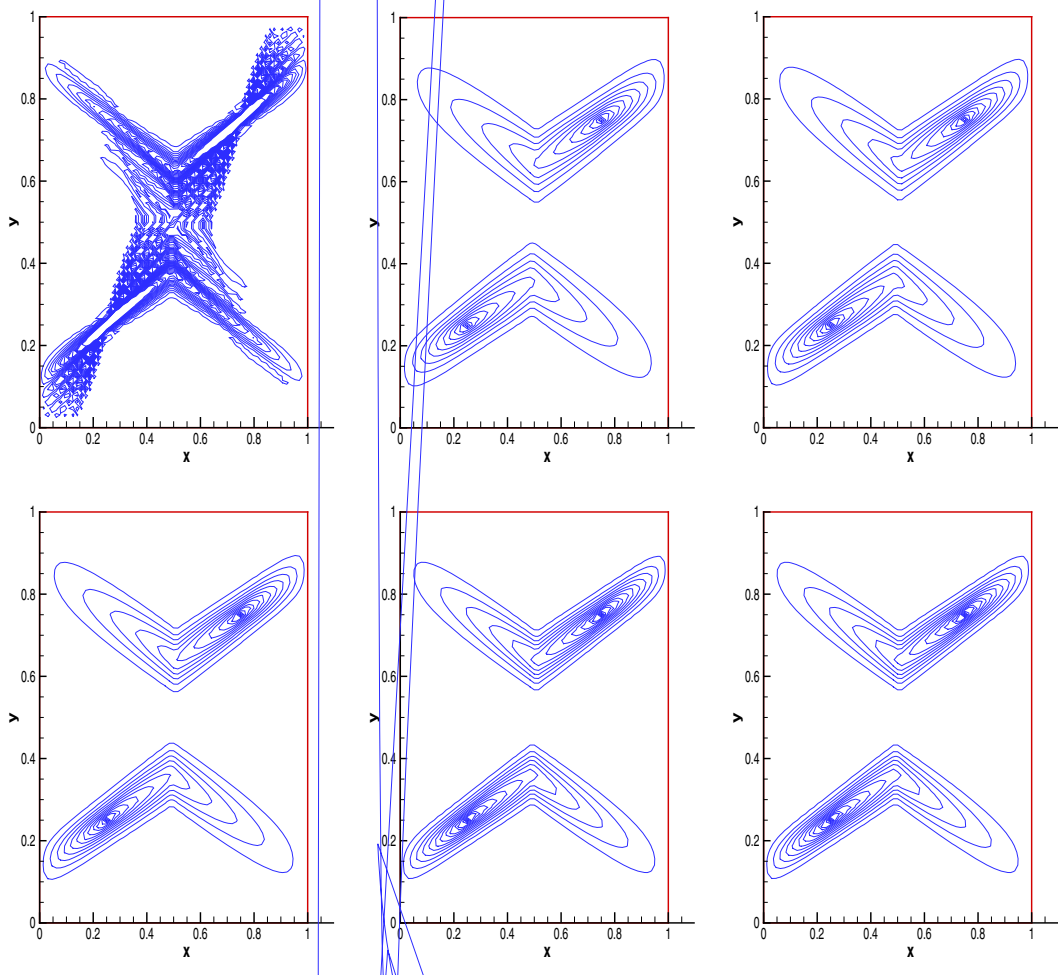

a scheme that self-adapts the discretization support locally according to the local orientation of the tensor field. The tests conducted show the optimal point yields results of sharper resolution than results corresponding to the first interval of the quadrature range.

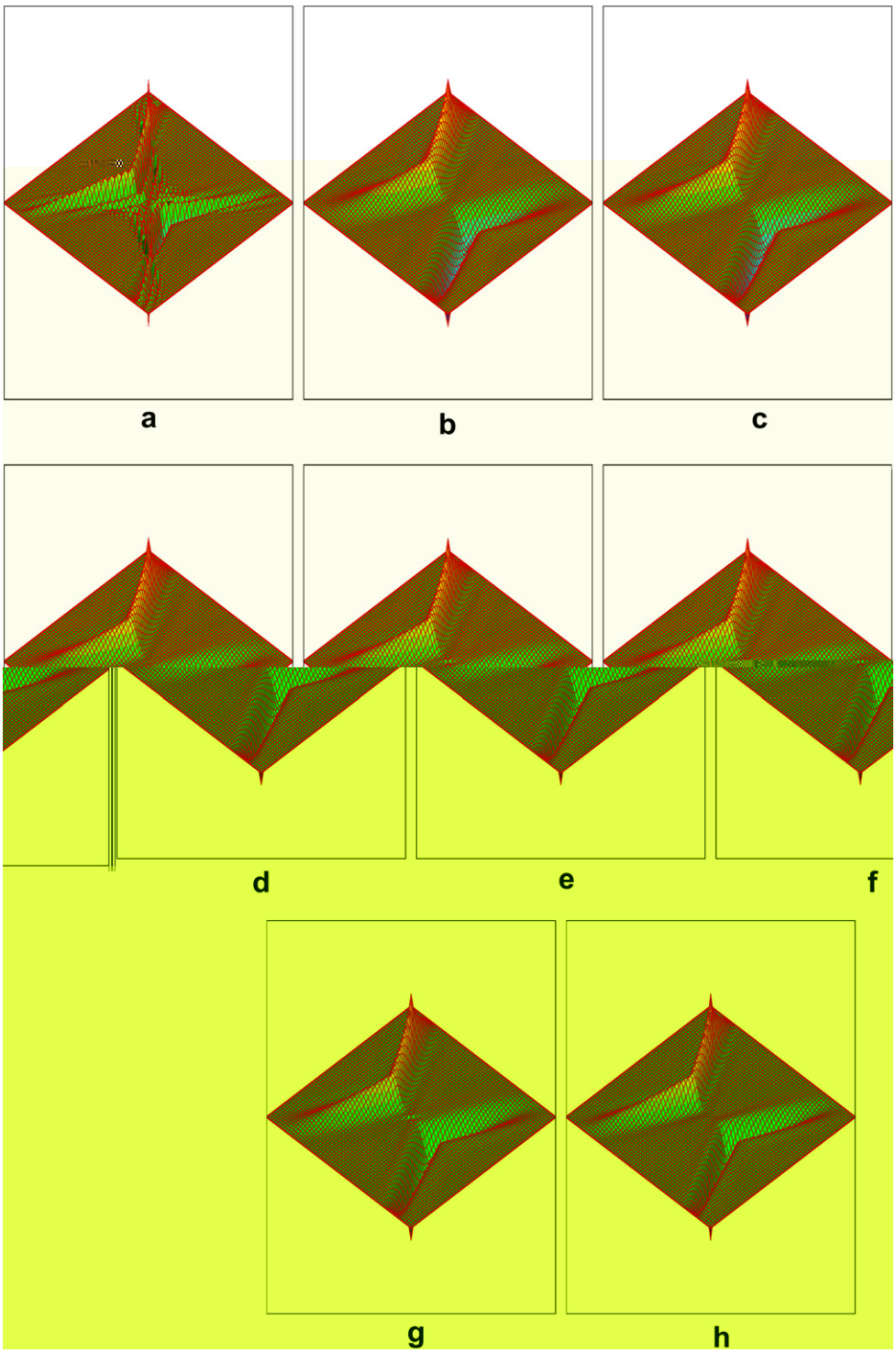

Fig. 25. Case 4: Iso-surface plot for 2×2 domain. (a) TPS $q = 1$. (b) FPS H scheme. (c) FPS $\eta = 0.25$. (d) FPS $\eta = \frac{1}{3}$. (e) FPS $\eta = \eta_{OS} - 15\%$. (f) FPS $\eta = \eta_{OS}$. (g) FPS $\eta = \eta_{OS} + 15\%$. (h) FPS $\eta = 0.45$.

For a spatially variable tensor field a locally upscaled tensor is used to define the local tensor dependent optimal quadrature point per dual-cell, the resulting finite-volume method is then applied to the original (non-upscaled) problem. In this case the scheme will have a quadrature point that lies in the neighbourhood of the exact optimal point. Tests of quadrature points within 15% (or slightly more) of the optimal point are found to yield results of comparable resolution to that of the optimal point, with similar sharper resolution.

Acknowledgments

The work of the first author is supported in part by EPSRC grant GR/S70968/01. The second author would like to thank ExxonMobil Upstream Research Company for supporting this project and permission to publish this work.

Appendix 1. Symmetric positive definite CVFE and FPS families

Symmetry of the cell-wise (or dual-cell) matrix for the CVFE family with cell-wise constant general tensor T follows if

$M_{ij} = M_{ji}$.

For example for $i = 1$, $i = 3$, assembling cell-wise flux contributions for the respective equations

$$\sum_{j=1}^{4} M_{1j}\phi_j = F_W + F_S$$

$$\sum_{j=1}^{4} M_{3j}\phi_j = -F_N - F_E$$

then identify the ϕ coefficients, e.g.

$$M_{13} = -\frac{1}{2}((T_{11} + T_{11})\eta + T_{12}) = M_{31}$$

and by inspection symmetry is verified. Symmetry of the discrete CVFE matrix follows from symmetry of the cell-wise matrix.

The discrete cell energy of the CVFE family is given by the inner product $\Phi^t M\Phi$ where $\Phi = (\phi_1, \phi_2, \phi_3, \phi_4)^t$. Using the CVFE flux definition of Eq. (22), the cell energy is expanded ([2])

$$\begin{aligned}\Phi^t M\Phi &= \phi_1(F_W + F_S) + \phi_2(F_E - F_S) - \phi_3(F_N + F_E) + \phi_4(F_N - F_W)\\ &= F_N(\phi_4 - \phi_3) + F_S(\phi_1 - \phi_2) + F_E(\phi_2 - \phi_3) + F_W(\phi_1 - \phi_4)\end{aligned}$$

and using the flux approximations of Eq. (22) the energy for the CVFE family for any quadrature point defined via η can be written as

$$\begin{aligned}\Phi^t M\Phi = \frac{1}{2}[&T_{11}(1-2\eta)(\phi_{21}^2 + \phi_{34}^2) + \eta(\phi_{21} + \phi_{34})^2 + T_{22}(1-2\eta)(\phi_{41}^2 + \phi_{32}^2) + \eta(\phi_{41} + \phi_{32})^2 + T_{12}(\phi_{21} + \phi_{34})\\ &\times(\phi_{41} + \phi_{32})],\end{aligned} \tag{59}$$

where $1 - 2\eta > 0$. Note that the double suffix of ϕ in Eq. (59) denotes a potential difference, e.g., $\phi_{21} = \phi_2 - \phi_1$. Using the identity $a^2 + b^2 \geqslant (a+b)^2/2$ it follows that

$$\Phi^t M\Phi \geqslant \frac{1}{4}(T_{11}x^2 + 2T_{12}xy + T_{22}y^2) \tag{60}$$

where $x = (\phi_{21} + \phi_{34})$ and $y = (\phi_{41} + \phi_{32})$, and it follows that the quadratic is positive with $T_{11} + 2T_{12}(y/x) + T_{22}(y/x)^2 \geqslant 0$ if $T_{12}^2 \leqslant T_{11}T_{22}$, i.e. T is elliptic. The Dirichlet condition ensures strict inequality. Therefore the CVFE family is symmetric positive definite for an elliptic cell-wise constant tensor if $\eta < 1/2$.

Since the FPS family coincides with the CVFE family for a spatially constant tensor, c.f. Section 7, it follows that the FPS family is SPD for a spatially constant tensor field.

Appendix 2. *H*-scheme coefficients

CVD(MPFA) $\eta = T_{22}/(T_{11} + T_{22})$ (FPS) H-scheme: Constant Tensor Field

Integer coordinates	Coefficients	Full tensor
i, j	M_{11}	$2(T_{11})$
$i+1, j$	M_{12}	$-T_{11} + T_{22}$
$i+1, j+1$	M_{13}	$-\frac{1}{2}T_{22} - \frac{1}{2}T_{12}$
$i, j+1$	M_{14}	0
$i-1, j+1$	M_{15}	$-\frac{1}{2}T_{22} + \frac{1}{2}T_{12}$
$i-1, j$	M_{16}	$-T_{11} + T_{22}$
$i-1, j-1$	M_{17}	$-\frac{1}{2}T_{22} - \frac{1}{2}T_{12}$
$i, j-1$	M_{18}	0
$i+1, j-1$	M_{19}	$-\frac{1}{2}T_{22} + \frac{1}{2}T_{12}$

References

[1] M.G. Edwards, C.F. Rogers, A flux continuous scheme for the full tensor pressure equation (section D) in: C.L. Farmer, Z.E. Heinemann (Eds.), Proceedings: 4th European Conference on the Mathematics of Oil Recovery, Norway, June 1994, pp. 194–208.
[2] M.G. Edwards, Symmetric, flux continuous, positive definite approximation of the elliptic full tensor pressure equation in local conservation form, in: 13th SPE Reservoir Simulation Symposium, San Antonio, Texas, USA, February 1995, pp. 553–562.
[3] M.G. Edwards, C.F. Rogers, Finite volume discretization with imposed flux continuity for the general tensor pressure equation, Comput. Geosci. (2) (1998) 259–290.
[4] M.G. Edwards, Unstructured, control-volume distributed, full-tensor finite volume schemes with flow based grids, Comput. Geosci. 6 (2002) 433–452.
[5] M.G. Edwards, Symmetric positive definite general tensor discretization operator on unstructured and flow based grids, paper E04, in: C.L.Farmer, Z.E. Heinemann (Eds.), Proceedings: 8th European Conference On Mathematics Of Oil Recovery, Freiberg, Germany, 3–6th September 2002, ISBN: 90-73781-24-8, pp. 22–32.
[6] M.G. Edwards, Control-volume distributed sub-cell flux schemes for unstructured and flow based grids, paper SPE 79710, in: SPE Reservoir Simulation Symposium, Houston, Texas, USA, 3–5 February 2003, 12 p., doi: 10.2118/79710-MS.
[7] M.G. Edwards, *M*-matrix flux splitting for general full tensor discretization operators on structured and unstructured grids, J. Comput. Phys. 160 (2000) 1–28.
[8] M.G. Edwards, M. Pal, Positive definite q-families of continuous subcell Darcy-flux CVD(MPFA) finite-volume schemes and the mixed finite element method, Int. J. Numer. Meth., Fluids 57 (2008) 355–387.
[9] M. Pal, M.G. Edwards, A.R. Lamb, Convergence study of a family of flux-continuous, finite-volume schemes for the general tensor pressure equation, Int. J. Numer. Meth., Fluids 51 (2006) 1177–1203.
[10] M. Pal, M.G. Edwards, Family of flux-continuous finite-volume schemes with improved monotonicity, paper B009, in: Proceedings of the 10th European Conference on the Mathematics of Oil Recovery, 4th–7th September 2006. ISBN:90-73781-47-7.
[11] M. Pal and M.G. Edwards, Flux-Splitting Schemes for improved monotonicity of discrete solution of elliptic equation with highly anisotropic coefficients, paper 384, in: Proceedings, ECCOMAS CFD-2006 Conference, Egmond aan Zee, The Netherlands, 5th–8th September, 2006. ISBN:90-9020970-0.
[12] M.G. Edwards, Higher-resolution hyperbolic-coupled-elliptic flux-continuous CVD schemes on structured and unstructured grids in 2-D, Int. J. Numer. Meth., Fluids 51 (2006) 1059–1077.
[13] M.G. Edwards, Higher-resolution hyperbolic-coupled-elliptic flux-continuous CVD schemes on structured and unstructured grids in 3-D, Int. J. Numer. Meth., Fluids 51 (2006) 1079–1095.
[14] I. Aavatsmark, T. Barkve, Ø. Bøe, T. Mannseth, Discretization on non-orthogonal, quadrilateral grids for inhomogeneous, anisotropic media, J. Comput. Phys. (127) (1996) 2–14.
[15] I. Aavatsmark, Introduction to multipoint flux approximation for quadrilateral grids, Comput. Geosci. (6) (2002) 405–432.
[16] S.H. Lee, H. Tchelepi, L.J. DeChant, Implementation of a flux continuous finite difference method for stratigraphic hexahedron, Grids SPEJ 7 (3) (2002) 267–277.
[17] S.H. Lee, P. Jenny, H.A. Tchelepi, A finite-volume method with hexahedral multiblock grids for modeling flow in porous media, Comput. Geo (6) (2002) 353–379.
[18] S. Verma, Flexible grids for reservoir simulation. Ph.D. Thesis, Stanford University, June, 1996.
[19] M.F. Wheeler, I. Yotov, A multipoint flux mixed finite element method, SIAM J. Numer. Anal. 44 (2006) 2082–2106.
[20] R.A. Raviart, J.M. Thomas, A Mixed Finite Element method for Second Order Problems, Lecture Notes in Mathematics 606, Springer-Verlag, New York, 1977.
[21] T.F. Russel, M.F. Wheeler, Finite element and finite difference methods for continuous flows in porous media, in: R.E. Ewing, Mathematics of Reservoir Simulation, Frontiers in Applied Mathematics SIAM 1983, pp. 35–106 (Chapter 2).
[22] C.L. Farmer, D.E. Heath, R.O. Moody, A global optimization approach to grid generation, in: 11th SPE Reservoir Simulation Symposium, Anaheim CA, USA, 17–20 February 1991, pp. 341–350.
[23] L.J. Durlofsky, A triangle based mixed finite element finite volume technique for modeling two phase flow through porous media, J. Comput. Phys. (1993) 252–266.
[24] T. Arbogast, M.F. Wheeler, I. Yotov, Mixed finite elements for elliptic problems with tensor coefficients as cell centered finite differences, SIAM J. Numer. Anal. 34 (2) (1997) 828.
[25] T.F. Russell, Relationships among some conservative discretization methods, in: Z. Chen et al. (Eds.), Numerical Treatment of Multiphase Flows in Porous Media, Lecture Notes in Physics, 552, Springer, Heidelberg, 2000, pp. 267–282.
[26] J.M. Hyman, M. Shashkov, S. Steinberg, The numerical solution of diffusion problems in strongly heterogeneous non-isotropic materials, J. Comput. Phys. 132 (1997) 130–148.
[27] B. Riviere, Discontinuous Galerkin method for solving the miscible displacement problem in porous media. Ph.D. Thesis, The University of Texas at Austin, 2000.
[28] B. Riviere, M.F. Wheeler, K. Banas, Discontinuous Glaerkin method applied to a single phase flow in porous media, Comput. Geosci. (4) (2000) 337–349.
[29] J.M. Nordbotten, G.T. Eigestad, Discretization on quadrilateral grids with improved monotonicity properties, J. Comput. Phys. 203 (2) (2005) 744–760.
[30] J.M. Nordbotten, I. Aavatsmark, Monotonoicity conditions for control volume methods on uniform parallelogram grids in homogeneous media, Comput. Geosci. 9 (2005) 61–72.
[31] J.M. Nordbotten, I. Aavatsmark, G.T. Eigestad, Monotonoicity of control volume methods, Numerische Mathematik 106 (2007) 255–288.
[32] M.J. Mlacnik, L.J. Durlofsky, Unstructured grid optimization for improved monotonocity of discrete solutions of elliptic equations with highly anisotropic coefficients, J. Comput. Phys. 216 (1) (2006) 337–361.
[33] M. Pal, M.G. Edwards, Quasi-monotonic continuous Darcy-flux approximation for general 3-D grids of any element type, paper SPE 106486, in: SPE Reservoir Simulation Symposium Houston, Texas, USA, 26–28 February 2007, 14 p., doi:10.2118/106486-MS.
[34] M.G. Edwards, Cross Flow, Tensors and finite volume approximation with deferred correction, Comput. Meth. Appl. Mech. Eng. 151 (1998) 143–161.
[35] P.I. Crumpton, G.J. Shaw, A.F. Ware, Discretization and multigrid solution of elliptic equations with mixed derivative terms and strongly discontinuous coefficients, J. Comput. Phys. 116 (1995) 343–358.
[36] M.G. Edwards, Superconvergent renormalization and tensor approximation, in: Proceedings: 5th European Conference on the Mathematics of Oil Recovery, Leoben Austria, 1996, 3–6 September, pp. 445–454. ISBN 3-9500542-0-0
[37] O. Axelsson, Iterative Solution Methods, Cambridge University Press, Cambridge, 1994.
[38] Q. Chen, J. Wan, Y. Yang, R. Mifflin, A new multi-point flux approximation for reservoir simulation, in: 106464 SPE Reservoir Simulation Symposium Houston, Texas, USA, 26–28 February 2007, doi:10.2118/106464-MS.
[39] H. Zheng, M.G. Edwards, M. Pal, Flux continuous finite volume schemes with full pressure continuity, in: Proceeding: 15th UK conference of ACME, Glasgow UK, April 2–3, 2007, pp. 48–57.
[40] R. Klausen, R. Winther, Convergence of multipoint flux approximations on quadrilateral grids, Numer. Meth. Part. Differ. Equations 22 (2006) 1438–1454.
[41] I. Aavatsmark, G.T. Eigestad, B.T. Mallison, J.M. Nordbotten, A compact multipoint flux approximation method with improved robustness, Numer. Meth. Part. Differ. Equations 24 (5) (2008) 1329–1360.
[42] K. Lipnikov, M. Shashkov, D. Svyatskiy, Yu. Vassilevski, Monotone finite volume schemes for diffusion equations on unstructured triangular and shape-regular polygonal meshes, J. Comput. Phys. 227 (2008) 492–512.